Laser-induced indirect ignition of non-premixed turbulent shear layers

Jonathan Wang[1], Mario Di Renzo[1], Gianluca Iaccarino[1,2], Hai Wang[2], Javier Urzay[3]

[1] *Center for Turbulence Research, Stanford University, Stanford, CA 94305*
[2] *Mechanical Engineering Department, Stanford University, Stanford, CA 94305*
[3] *US Space Force at Rocket Propulsion Division, Air Force Research Laboratory, Edwards AFB, CA 93526*

Abstract

This study uses direct numerical simulations to investigate the forced ignition of temporally-evolving turbulent subsonic shear layers separating a gaseous stream of methane (CH_4) and a stagnant gas environment of molecular oxygen (O_2). Ignition is forced by a thermal-energy source that heats up a small volume of gas during periods of time much shorter than the characteristic acoustic time scale. The kernel, including its initial rounded conical shape, resembles experimental observations after optical breakdown is achieved in a gas irradiated by a focused laser. Particular emphasis is placed on ignition phenomena observed when the laser is focused on the O_2 environment outside the turbulent shear layer, where the local composition is far beyond the lean flammability limit. This represents an indirect mode of non-premixed ignition that develops after a relatively long period of time has passed since laser-energy deposition, when the eddies near the oxidizer edge of the turbulent shear layer are intercepted by a baroclinically-generated subsonic vortex of hot dissociated O_2 ejected from the laser-energy deposition zone. The success of indirect ignition depends on the orientation of the laser beam, the thickness of the shear layer, and the kernel standoff distance from the oxidizer edge of the shear layer. An ignition Damköhler number is defined that accounts for these averaged effects in six different simulation cases. For near-unity ignition Damköhler numbers, the solution is also sensitive to the local instantaneous flow field prevailing near the oxidizer edge of the shear layer, in that a modification of the instantaneous pre-deposition flow field, while preserving its turbulence statistics, can produce different ignition outcomes.

Keywords: Non-premixed ignition, Turbulent combustion, Direct numerical simulations

1. Introduction

With the advent of miniaturization of laser systems and an increased need for rapid in-space maneuvering, renewed interest in laser-based forced ignition has arisen for re-startable bipropellant rocket engines of upper stages and reaction control thrusters of spacecrafts [1–13]. This study addresses a fundamental problem associated with the development of this technology, namely the ignition of a non-premixed turbulent shear layer forced by laser-energy deposition.

In prototype rocket-propulsion applications of laser-induced ignition, a Nd:YAG laser pulse of approximately $t_L \sim 10$ ns, with a wavelength of about 1 μm, is focused into a small spot of approximate size $L \sim 1$ mm in a combustor primed with propellants injected at temperatures much lower than typical crossover values [8]. The laser delivers an energy $E \sim 10 - 100$ mJ in the focal region, which is equivalent to a power density of 10-100 GW/cm^2 that ionizes the propellants and creates a small pocket of plasma at temperatures exceeding 30,000 K [14].

The characteristic acoustic time across the pocket $t_a = L/a_\infty \sim 1$ μs, with a_∞ being the speed of sound in the gas surrounding the pocket, is typically much larger than t_L, and therefore the energy is deposited nearly isochorically engendering high pressures in the deposition zone [5, 15, 16]. Shortly after, the plasma begins thermalizing and recombining into a hot electroneutral gas while expanding itself via an outwardly propagating shock wave [17–19]. For laser ignition of typical hydrocarbon fuels premixed with oxidizers, the characteristic ignition time t_{ig} is much larger than the acoustic time t_a. Consequently, ignition starts to develop after the blast wave has weakened and propagated to distances $Lt_{ig}/t_a \gg L$ away from the region of interest [13, 16, 20].

The initial kernel size L obtainable with practical laser sources is typically comparable to or larger than that of large-scale eddies in turbulent shear layers near propellant injectors. As a result, the relative large value of the characteristic molecular diffusion time across the kernel, $t_c = L^2/\nu_\infty \sim 100$ ms, with ν_∞ being the kinematic viscosity of the ambient gas, indicates that heat conduction does not play any significant role in decreasing the kernel temperature across scales comparable to L during the entire ignition process. Instead, as explained below, the kernel is deformed and stretched considerably because of a self-induced baroclinic vortical gas motion, which convectively mixes the hot gas with its environment over time scales that are much shorter than t_c but comparable to t_{ig} [13, 15, 16, 21–28]. This hydrodynamic effect complicates the description of laser-induced ignition in rocket engines and fundamentally separates the problem studied here from that of concentrated or spherico-symmetric ignition kernels in stagnant mixtures [29, 30].

Whether the aforementioned physical process leads to successful forced ignition in the combustor depends on many parameters, including the local aerothermochemical conditions of the propellants in the focal region and the amount of energy E deposited by the laser, which needs to be larger than a threshold in order to induce a post-expansion temperature higher than the crossover value [30–32]. An extra factor to consider is the presence of turbulence and mean composition gradients, both of which are ubiquitous in practical applications [33, 34]. Too intense turbulence strains the kernel and transports thermal energy away over times shorter than t_{ig}, thereby hindering combustion even for energies above the minimum ignition value [12, 35–37]. As a result, the dynamics and final outcome of laser-energy deposition are typically accompanied with significant stochasticity in practical configurations [7, 13, 38–41].

A complex electrohydrodynamic coupling between the laser and the ensuing plasma arises early in the process during the first few nanoseconds of energy deposition and involves an electron runaway and the inverse of bremsstrahlung [42]. The characteristic time scales for transport and neutral chemistry in combustors of chemical propulsion systems are several orders of magnitude larger than those involved in the laser-plasma coupling [17, 18]. As a result, numerical simulations of the full deposition-to-ignition process are exceedingly costly. A standard approximation that circumvents this challenge is to assume that the hot gas kernel is composed solely of electroneutral species at the laser focal point upon depositing the energy [3, 35, 37, 38, 43]. This approach, which is also employed in this study and resolves neither the propagation of the laser nor the generation of the plasma, assumes a separation of time scales such that the laser-plasma coupling occurs infinitely fast compared to the acoustic time t_a. Equivalently, the plasma has fully recombined by the time the kernel begins to expand. Effects of remnant charged species are therefore neglected during the initial stage of radical chain branching, although they may well lead to acceleration of the ignition chemistry [44].

Perhaps the most surprising outcome of the early laser-plasma coupling is the complex shape of the resulting kernel observed in experiments and simulations [13, 16, 18]. In particular, the kernel adopts an axisymmetric, rounded conical shape with two differently sized lobes. The axis of the kernel is aligned with the laser beam, with the lobe closest to the laser source typically being larger than the other lobe. This observation was explained by Raizer and is based on a wave of light absorption and gas heating that propagates in the direction opposite to the converging laser beam after the primary breakdown has occurred [45]. The resulting early plasma pocket has the shape of a truncated cone, which later becomes an rounded cone or ovoid due to expansion.

The significant departures from spherical symmetry in the kernel, in conjunction with the expansion due to the outgoing blast wave, engenders vorticity baroclinically and leads to the unexpected outcome shown in Fig. 1, which corresponds to experiments reported in Ref. [13]. An ignition event is observed there despite the fact that the laser is focused on the oxidizer environment. Specifically, ignition appears to be aided by an ejecta emanating from the kernel and impinging on the turbulent shear layer. Note that although this effect may be enhanced by the entrainment in the shear layer, the ejecta develops independently of that, as observed experimentally in stagnant gases [13, 16, 19].

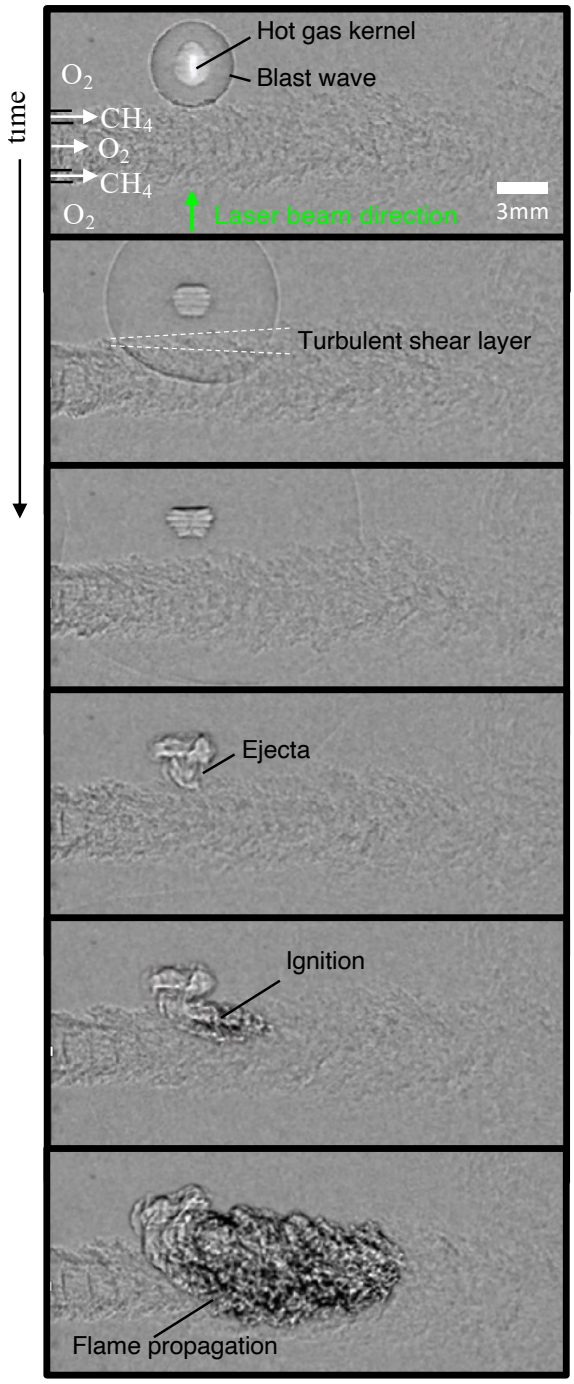

Figure 1: Experimental Schlieren visualizations of laser-induced indirect ignition in a subscale rocket combustor. The configuration consists of a subsonic O_2 central jet surrounded by a near-sonic annular coflow of CH_4, both being at room temperature and discharging into an environment primed with O_2 at near-atmospheric pressure. The laser beam propagates upwardly as indicated in the figure. It consists of a single pulse of wavelength 532 nm from a flashlamp pumped Nd:YAG laser depositing 26 mJ into a focal region of approximate width of 600 μm in the O_2 environment. Images are courtesy of Prof. Carson Slabaugh at Purdue University. Further details can be found in Ref. [13].

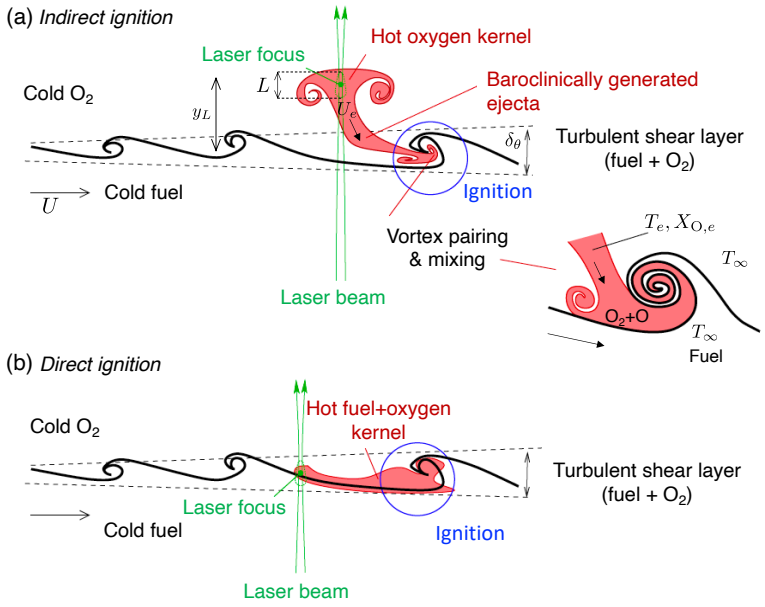

Figure 2: Schematics of (a) indirect and (b) direct ignition modes for non-premixed turbulent shear layers depending on location of the laser focus.

The ignition mode resulting from the laser being focused outside the shear layer, clearly beyond the flammability limits as in Figs. 1 and 2(a), is referred to as indirect ignition and is at the center of the present study. In contrast, the classic direct ignition mode refers to that observed when the laser is focused directly on the shear layer, where fuel and oxidizer coexist, as depicted in Fig. 2(b), and is not considered further in this work.

In this study, direct numerical simulations (DNS) are employed to investigate the indirect ignition of turbulent shear layers by focusing the laser on the O_2 environment in a configuration similar to Fig. 2(a), which requires consideration of the baroclinically generated ejecta and its interaction with the eddies in the shear layer. This extends the simulations in Ref. [43] by including complex chemistry and thermophysical properties along with realistic kernel shapes. It also complements the simulations in Ref. [46] by incorporating turbulence effects.

The remainder of this paper is organized as follows. Details of the formulation and computational setup are outlined in Sec. 2. DNS results are provided in Sec. 3 for cases involving variations of standoff distance, time of laser-energy deposition, along with variations in the pre-deposition flow field. Lastly, conclusions are given in Sec. 4. Three auxiliary sections are included in the Supplementary Material with details about boundary conditions, chemical kinetics, and simulation movies.

2. Formulation and computational setup

In this section, a description of the model problem for laser-induced indirect ignition is provided along with the associated formulation, boundary conditions and physical parameters.

2.1. Regime of interest

Because of relevance for practical applications, the regime studied here corresponds to

$$y_L > L > \delta_\theta, \tag{1}$$

$$t_L \ll t_a < \delta_\theta/U < y_L/U_e \ll t_c, \tag{2}$$

and

$$E/(\rho_{O_2,\infty} V_L) \gg a^2_{O_2,\infty}/[\gamma_{O_2,\infty}(\gamma_{O_2,\infty} - 1)]. \tag{3}$$

In these equations, δ_θ is the momentum thickness of the shear layer, y_L is the laser-focus standoff distance measured from the shear-layer centerline, V_L is the initial volume of the kernel, U is the fuel-stream velocity, and U_e is the ejecta velocity, as depicted in Fig. 2(a). In addition, $\rho_{O_2,\infty}$, $a_{O_2,\infty}$, and $\gamma_{O_2,\infty}$ are, respectively, the density, speed of sound, and adiabatic coefficient in the O_2 environment. The rest of the parameters are defined in Sec. 1.

The ejecta velocity U_e is an intricate function of the characteristic specific energy deposited in the gas $E/(\rho_{O_2,\infty} V_L)$ and needs to be determined numerically. In all cases studied here, the specific kinetic energy associated with the ejecta, $U_e^2/2$, is less than 0.01% of the deposited specific energy. The latter is much larger than the initial specific internal energy of the gas, $a^2_{O_2,\infty}/[\gamma_{O_2,\infty}(\gamma_{O_2,\infty}-1)]$. Consequently, the relative temperature increment induced by the laser on the gas during the deposition time, $\Delta T/T_\infty \sim E\gamma_{O_2,\infty}(\gamma_{O_2,\infty} - 1)/(\rho_{O_2,\infty} V_L a^2_{O_2,\infty})$, is a large quantity that attains values of order 10^2. However, as shown in these simulations, the early expansion of the kernel cools significantly this hot gas and partially recombines it over short time scales comparable to t_a. After that, the baroclinically generated ejecta is fully formed and continues carrying the hot gas toward the shear layer over a time scale comparable to the large-eddy turnover time δ_θ/U. The ejecta becomes increasingly stretched as it moves toward the shear layer, which further cools down the gas. The ejecta has modest temperatures $T_e \sim 1000 - 1200$ K when it intercepts the shear layer, but contains atomic oxygen in super-equilibrium molar factions $X_{Oe} \sim 0.1 - 0.2$ sufficient to induce ignition, as will be discussed below in Sec. 3.

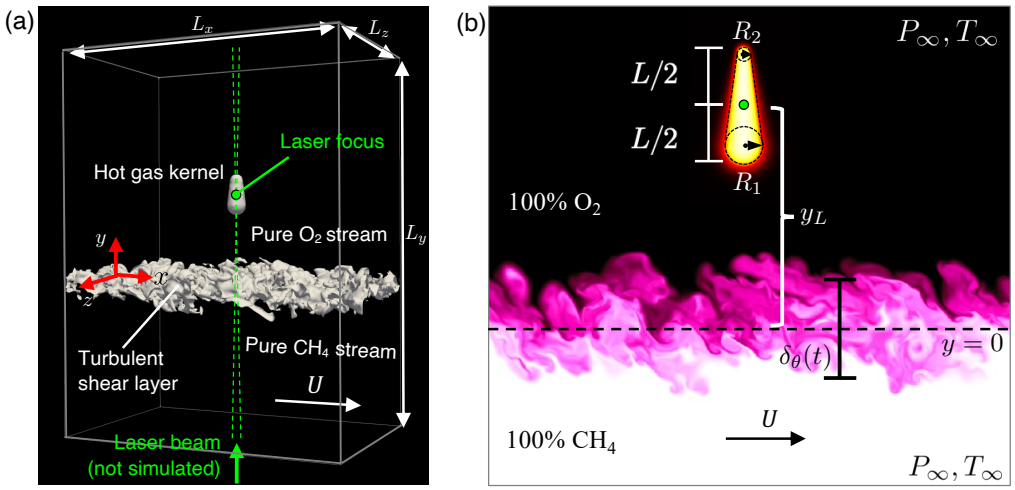

Figure 3: (a) Schematics of the model problem and (b) $z = 0$ slice of the computational domain at the time of energy deposition.

2.2. The model problem

The configuration in Fig. 3(a) is used here to study indirect ignition in a canonical scenario reminiscent of Fig. 2(a). The computational setup consists of a biperiodic, isothermal, turbulent shear layer developed between a pure gaseous CH_4 stream moving to the right at subsonic velocity U, and a pure gaseous O_2 stagnant environment on which the laser is focused after propagating upwardly across the shear layer. Note that in this temporally-evolving configuration the shear layer grows while the kernel develops, whereas in the spatially evolving problem described in Fig. 2(a) the shear layer does not grow at the streamwise location of the kernel if the O_2 environment is at rest and therefore cannot advect the kernel downstream. Despite this shortcoming, it will be shown below that the conditions influencing the ignition dynamics are those at ejecta/shear-layer interception, and therefore the history of the shear layer until the time of interception is inconsequential. After that, successful ignition occurs faster than the large-eddy turnover time. As a result, the shear layer grows only by less than 1% from interception to ignition [see Eq. (14) introduced below]. The choice of this configuration is clearly driven by affordability because of the exceedingly high cost of simulating the spatial development of the shear layer using DNS for multiple cases.

In this configuration, the far-field temperature and pressure are equal to $T_\infty = 300$ K and $P_\infty = 1$ atm, respectively, thereby giving a fuel-to-oxidizer density ratio $\rho_{CH_4,\infty}/\rho_{O_2,\infty} = 1/2$. The corresponding convective Mach number is in the low subsonic range, $Ma_c = U/(a_{O_2,\infty} + a_{CH_4,\infty}) = 0.07$, where $a_{O_2,\infty}$ and $a_{CH_4,\infty}$ are the speed of the sound waves in the oxidizer and fuel streams, respectively. A Cartesian reference frame $\{x, y, z\}$ is defined in which x is aligned with the motion of the CH_4 stream, y is normal to the mean plane of the shear layer, and z is in the spanwise direction, with $z = 0$ being the midsection plane. As mentioned above, the propagation of the laser beam and the ensuing plasma pocket are not treated in these simulations. Instead, following a method described below, an amount of thermal energy is deposited quasi-instantaneously within a rounded conical region of longitudinal size L centered at $x = L_x/2$, $y = y_L$, and $z = 0$, as depicted in Fig. 3(b).

2.3. Conservation equations

The DNS is carried using the Hypersonics Task-based Research (HTR) solver [47]. This code integrates the multicomponent Navier-Stokes equations

$$\frac{\partial \rho Y_k}{\partial t} + \nabla \cdot (\rho Y_k \mathbf{v}) = -\nabla \cdot (\rho Y_k \, \mathbf{V}_k) + \dot{w}_k, \quad k = 1, \dots N_s, \tag{4}$$

$$\frac{\partial \rho \mathbf{v}}{\partial t} + \nabla \cdot (\rho \mathbf{v}\mathbf{v}) = -\nabla P + \nabla \cdot \boldsymbol{\tau}, \tag{5}$$

and

$$\frac{\partial}{\partial t}\left[\rho\left(e + \frac{|\mathbf{v}|^2}{2}\right)\right] + \nabla \cdot \left[\rho \mathbf{v}\left(e + \frac{|\mathbf{v}|^2}{2}\right)\right] = -\nabla \cdot (P\mathbf{v}) + \nabla \cdot (\boldsymbol{\tau} \cdot \mathbf{v}) - \nabla \cdot \boldsymbol{q} + \dot{Q}_L. \tag{6}$$

In this formulation, ρ is the density, P is the thermodynamic pressure, N_s is the number of species, e is the specific internal energy (including both thermal and chemical energy), and $\mathbf{v} = \{u, v, w\}$ is the velocity vector in the Cartesian coordinate system $\{x, y, z\}$ depicted in Fig. 3(a). Additionally, Y_k, $\dot{w}_k$, and $\mathbf{V}_k$ are, respectively, the mass fraction, chemical production rate per unit volume, and diffusion velocity vector of species k, the latter being given by [48, 49]

$$\mathbf{V}_k = -D_k \nabla (\ln X_k) + \sum_{j=1}^{N_s} Y_j D_j \nabla \left(\ln X_j\right), \tag{7}$$

where X_k and D_k are the molar fraction and molecular diffusion coefficient of species k, respectively. Barodiffusion and thermal-diffusion effects are neglected in writing Eq. (7). These effects may be the subject of future work as they could be important for the transport of dissociated species in the early stages of energy deposition $t \ll t_a$, when gradients of both temperature and pressure are high due to the proximity of the blast

wave to the kernel. In Eqs. (5) and (6), the symbols $\boldsymbol{\tau}$ and $\boldsymbol{q}$ refer to the viscous stress tensor

$$\boldsymbol{\tau} = 2\mu\boldsymbol{S} - \frac{2}{3}\mu(\nabla\cdot\mathbf{v})\boldsymbol{I} \tag{8}$$

and heat flux

$$\boldsymbol{q} = -\lambda\nabla T + \sum_{k=1}^{N_s}\rho Y_k h_k \mathbf{V}_k. \tag{9}$$

In these equations, μ is the dynamic viscosity, $\boldsymbol{S} = (\nabla\mathbf{v}+\nabla\mathbf{v}^T)/2$ is the strain-rate tensor, $\boldsymbol{I}$ is the identity tensor, T is the static temperature, λ is the thermal conductivity, and h_k is the specific enthalpy of species k. The transport coefficients μ, λ, and D_k are calculated as follows: μ is computed with Wilke's mixing rule [50], λ with the mixing rules described in Refs. [51, 52], and D_k with the Hirschfelder-Curtiss approximation [53]. Additional details of the formulation can be found in Ref. [47].

The chemical production rate $\dot{w}_k$ is evaluated with a 35-step, 12-species CH_4/O_2 electroneutral chemical-kinetic reduced mechanism FFCMy-12 extended to near-atmospheric pressures. The initial version of this model was based on a trial version of the Foundational Fuel Chemistry Model [54] and subsequently tested for laminar premixed-flame speed, ignition delay, and extinction time in CH_4/O_2 and CH_4/air mixtures at elevated pressures higher than 10 atm. DNS of turbulent premixed CH_4/O_2 flames at 30 atm over a wide range of Karlovitz numbers were also demonstrated using this model [55]. In the present study, this model has been optimized to better reproduce the laminar premixed-flame speed and homogeneous ignition delay of CH_4/O_2 mixtures at near-atmospheric pressures, as detailed in Sec. S1 of the Supplementary Material. The species in the model are $CH_4, CH_3, CH_2O, CO_2, CO, O_2, O, H_2, H, OH, HO_2$, and H_2O. The choice of this reduced mechanism is a compromise between computational cost and a minimum level of physical fidelity that does not produce artifacts. An example of the latter would be the unrealistically high post-expansion temperatures that would be obtained using too compact kinetic descriptions such as a single-step mechanism because of ignoring the dissociation of O_2, which would also neglect the effect of O atoms on ignition. These are critical considerations for laser-induced indirect ignition, as will be explained in Sec. 3.

The specific internal energy e and specific enthalpy h_k are calculated using NASA polynomials [56, 57]. In particular, the 7-coefficient NASA parameterization in Ref. [56] is kept in its original form for $T \leq 5{,}000$ K. However, due to the high initial temperature generated by the energy deposition, the 9-coefficient parameterization in Ref. [57] is recalibrated based on the rigid-rotor harmonic-oscillator approximation for $5{,}000\ \text{K} < T \leq 50{,}000$ K. This high-temperature stage is short-lived due to the rapid expansion of the kernel, and does not overlap with the ignition stage that may ensue later. For instance, the temperature in the kernel drops to values of order 5,000 K after approximately 1 μs has passed since the laser-energy deposition, whereas ignition and combustion require, at least, an additional 100 μs.

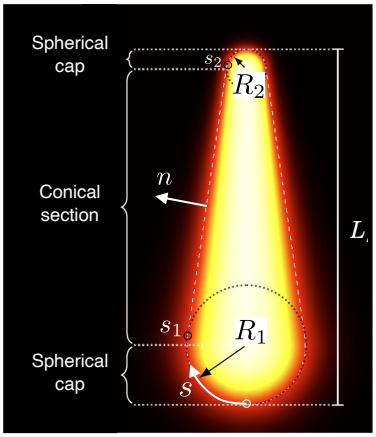

Figure 4: Meridian cross-section of the contours of the axisymmetric model function $f(n)$ defining the initial rounded conical shape of the kernel represented by the energy source (11).

The formulation presented above is supplemented with the equation of state for a multicomponent mixture of ideal gases,

$$P = \rho \mathrm{R}^0 T/W. \tag{10}$$

In this formulation, R^0 is the universal gas constant and $W = (\sum_{k=1}^{N_s} Y_k/W_k)^{-1}$ is the average molecular weight of the mixture, with W_k being the molecular weight of species k.

2.4. Laser-induced source of thermal energy

The symbol $\dot{Q}_L$ in Eq. (6) represents the rate of laser-induced deposition of thermal energy per unit volume,

$$\dot{Q}_L = \rho \dot{e}_L f(n) g(t). \tag{11}$$

In Eq. (11), the symbol $\dot{e}_L$ is a parameter representing the rate of deposition of thermal energy per unit mass that is chosen to satisfy the integral balance $E = \int\int \dot{Q}_L dt dV$, with E being the target energy value deposited by the laser in the gas. In addition, $\dot{Q}_L$ is windowed in time by the Gaussian function

$$g(t) = \exp\left[-(t-t_d)^2/(2t_L^2)\right], \tag{12}$$

where t_L is the laser pulse duration and t_d is the time of laser-energy deposition measured from simulation start $t = 0$.

As indicated in Fig. 4, the rounded conical shape of the kernel is imposed by an axisymmetric monotonically-decreasing function of the local coordinate n normal to the kernel, $f(n)$, with $f = 1$ in the kernel and $f = 0$ outside [58]. The form of f is chosen as $f(n) = (1/2)[1 - \tanh(bn)]$, with b being a parameter such that $f[-c(s)/2] = 0.9$ and $f[c(s)/2] = 0.2$, where $c(s)$ is a piecewise function of the local coordinate s tangential to the kernel that satisfies $c = R_1$ for $s \leq s_1$, $c = (s-s_2)R_1/(s_1-s_2) + (s-s_1)R_2/(s_1-s_2)$ for $s_2 > s > s_1$, and $c = R_2$ for $s \geq s_2$. In this formulation, s_1 and s_2 are functions of L, R_1, and R_2, and correspond to values of s at the points of tangency between the spherical caps and the central conical section of the kernel.

Description	Symbol [units]	Value
Deposited laser energy	E [mJ]	16.7
Laser pulse duration	t_L [ns]	6.5
Kernel length	L [mm]	1.5
Kernel large radius	R_1 [mm]	0.3
Kernel small radius	R_2 [mm]	0.15
Freestream fuel velocity	U [m/s]	54.6
Ambient pressure	P_∞ [atm]	1.0
Ambient temperature	T_∞ [K]	300
Initial vorticity thickness	$\delta_{\omega,0}$ [mm]	0.20
Initial momentum thickness	$\delta_{\theta,0}$ [mm]	0.05

Table 1: Relevant dimensional simulation parameters applicable to all simulation cases considered in this study.

2.5. Averaging operations

The Reynolds average of any quantity φ is denoted by an overbar and is defined as the average in the homogeneous directions x and z, namely $\overline{\varphi} = \int_{-L_z/2}^{+L_z/2} \int_0^{L_x} \varphi dx dz/(L_x L_z)$, whereas its perturbation from the mean is denoted by φ'. Similarly, the Favre average of φ is obtained by computing $\widetilde{\varphi} = \overline{\rho\varphi}/\overline{\rho}$, with φ'' being the corresponding Favre fluctuation.

In this configuration, statistical averaging along homogeneous directions is relevant only initially before the laser-energy deposition, $t < t_d$, and after long times $t \gg t_{ig}$ when a diffusion flame is established if ignition is successful. During the ignition development, $t_d < t \sim t_{ig}$, which is the phase this study focuses on, any space-based statistical average obscures localized mixing and ignition phenomena. The correct averaging procedure during this intermediate stage would require a sufficiently large number of realizations to warrant statistical convergence of an ensemble average, which is unfeasible from a DNS cost standpoint and would instead demand the use of large eddy simulations (LES) with associated subgrid-scale models. That is an endeavor reserved for future work since it first requires fundamental knowledge at DNS level.

2.6. Initial and boundary conditions

The formulation outlined in Secs. 2.3 and 2.4 is integrated subject to the following initial and boundary conditions. The boundary layer is initialized with a Reynolds mean velocity field characterized by $\overline{v} = \overline{w} = 0$, whereas $\overline{u}$ only depends on y as $\overline{u} = (U/2)[1 - \tanh(2y/\delta_{\omega,0})]$, with $\delta_{\omega,0}$ corresponding to the initial value of the vorticity thickness $\delta_\omega \equiv U/\max\{\partial\overline{u}/\partial y\}$. In order to induce transition to turbulence, three-dimensional isotropic velocity fluctuations $\{u', v', w'\}$ with a turbulent intensity of 5% are added to the mean velocity profile using the model spectrum for homogeneous incompressible turbulent flows described in Ref. [59]. These initial fluctuations are spatially localized in the mixing region using a Gaussian windowing function centered at $y = 0$ with a standard deviation of $\delta_{\omega,0}$.

The oxidizer and fuel mass fractions are initialized with zero fluctuations as $Y_{O_2} = 1 - (1/2)[1 - \tanh(2y/\delta_{\omega,0})]$ and $Y_{CH_4} = [1/(2S)][1 - \tanh(2y/\delta_{\omega,0})]$, with $S = 4$ being the mass of oxidizer per unit mass of fuel in stochiometric proportions. In this way, the isoline of unity equivalence ratio $\phi = S\,Y_{CH_4}/Y_{O_2} = 1$ initially corresponds to $y = 0$. Using these initial conditions, the initial profile of density can be obtained from Eq. (10) by imposing uniform values of pressure P_∞ and temperature T_∞.

Before depositing the laser energy, periodic boundary conditions are employed along the homogeneous directions at $x = 0$, $x = L_x$, and $z = \pm L_z/2$. One-dimensional non-reflecting Navier-Stokes characteristic boundary conditions (NSCBCs) are applied at the top and bottom boundaries located at $y = 5L_y/8$ and $y = -3L_y/8$, respectively [60, 61]. These are standard boundary conditions shown to capture the dynamics of temporally-evolving turbulent shear layers [62, 63].

After depositing the laser energy, the boundary conditions are momentarily replaced with a sponge that absorbs the blast wave in order to avoid its artificial reflection from the y boundaries (because of the inherent partial reflectivity of the NSCBCs) or return into the domain through the x and z boundaries (because of periodicity). This sponge acts rapidly in times of the order of $L_x/a_{O_2,\infty}$ as the shock crosses a thin region adjacent to the boundaries, and is deactivated thereafter. The thicknesses of this region, where the sponge is active, are $0.03L_x$, $0.02L_y$, and $0.05L_z$ for the streamwise, transverse, and spanwise boundaries, respectively. Further details are provided in Sec. S2 of the Supplementary Material, including an analysis that shows insensitivity of the turbulence statistics of the shear layer to the activation and deactivation of the sponge.

2.7. Simulation parameters

The main parameters of the simulation are listed in Tables 1 and 2 in dimensional and dimensionless forms, respectively. To compute these parameters, use has been made of the definition of momentum thickness

$$\delta_\theta = \frac{2}{(1 + \rho_{CH_4,\infty}/\rho_{O_2,\infty})} \int_{-\infty}^{\infty} \frac{\overline{\rho}\widetilde{u}}{\rho_{O_2,\infty} U} \left(1 - \frac{\widetilde{u}}{U}\right) dy, \qquad (13)$$

which is a quantity that increases with time. As a result, Tables 1 and 2 quote values of characteristic parameters at $t = 0$ (denoted by a subindex 0) and a representative end time $t^* U/\delta_{\theta,0} = 422$ (denoted by an asterisk). The total simulation time varies per case, as explained in Sec. 3, with the longest one lasting until approximately $tU/\delta_{\theta,0} = 650$, or equivalently, 0.6 ms. In this way, the momentum and vorticity Reynolds numbers vary from $Re_{\theta,0} = U\delta_{\theta,0}/\nu_{O_2,\infty} = 177$ and $Re_{\omega,0} = U\delta_{\omega,0}/\nu_{O_2,\infty} = 663$ initially when the flow is laminar, to $Re^*_\theta = U\delta^*_\theta/\nu_{O_2,\infty} = 1281$ and $Re^*_\omega = U\delta^*_\omega/\nu_{O_2,\infty} = 5955$ at the representative end time when the flow is turbulent. The corresponding Taylor-Reynolds number at the representative end time is $Re^*_\lambda = 2k\sqrt{5/(\overline{\nu}\epsilon)} = 47$, where k is the turbulent kinetic energy and ϵ is the turbulent dissipation.

Figure 5 shows the approximate asymptotic self-similarity observed at sufficiently long simulation times for the turbulent shear layer alone. In particular, approximate collapses of first and second-order statistics are shown in Fig. 5(a-c). These are accompanied by the quasi-linear growth rate of δ_θ shown in Fig. 5(d) for $tU/\delta_{\theta,0} \gtrsim 190$, which can be described by

$$\delta_\theta \sim C_1 U t, \qquad (14)$$

with $C_1 \simeq 0.0159$. Except for the case involving the isolated kernel, in all other cases considered in Sec. 3 the position y_L

Description	Symbol	Value
Initial vorticity Reynolds number	$Re_{\omega,0}$	663
Initial momentum Reynolds number	$Re_{\theta,0}$	177
Representative-end-time vorticity Reynolds number	Re^*_ω	5955
Representative-end-time momentum Reynolds number	Re^*_θ	1281
Representative-end-time Taylor-Reynolds number	Re^*_λ	47
Ratio of vorticity thickness to kernel size	δ^*_ω/L	1.21
Ratio of momentum thickness to kernel size	δ^*_θ/L	0.26
Convective Mach number	Ma_c	0.07
Freestream oxidizer Mach number	Ma_{O_2}	0.17
Freestream fuel Mach number	Ma_{CH_4}	0.12
Ratio of laser specific energy to initial gas specific internal energy	$[E\gamma_{\mathrm{O}_2,\infty}(\gamma_{\mathrm{O}_2,\infty}-1)]/(\rho_{\mathrm{O}_2,\infty}V_L a^2_{\mathrm{O}_2,\infty})$	278
Ratio of acoustic time to laser-pulse duration	t_a/t_L	692
Ratio of integral time to acoustic time	$\delta^*_\theta/(Ut_a)$	1.6
Kernel aspect ratio	$L/(2R_1)$	2.5
Kernel extrema radii ratio	R_1/R_2	2
Fuel-to-oxidizer density ratio	$\rho_{\mathrm{CH}_4,\infty}/\rho_{\mathrm{O}_2,\infty}$	0.5
Stoichiometric mixture fraction	Z_{st}	0.2
Ratio of Kolmogorov length to grid size	$\min(\eta^*)/\Delta x$	0.59
Ratio of laminar premixed-flame thickness to grid size	$\delta_f/\Delta x$	6.4
Number of streamwise integral lengths in the domain	L_x/ℓ^*_x	28
Number of spanwise integral lengths in the domain	L_z/ℓ^*_z	58
Number of momentum thicknesses in the domain	L_y/δ^*_θ	27

Table 2: Relevant dimensionless simulation parameters applicable to all simulation cases considered in this study.

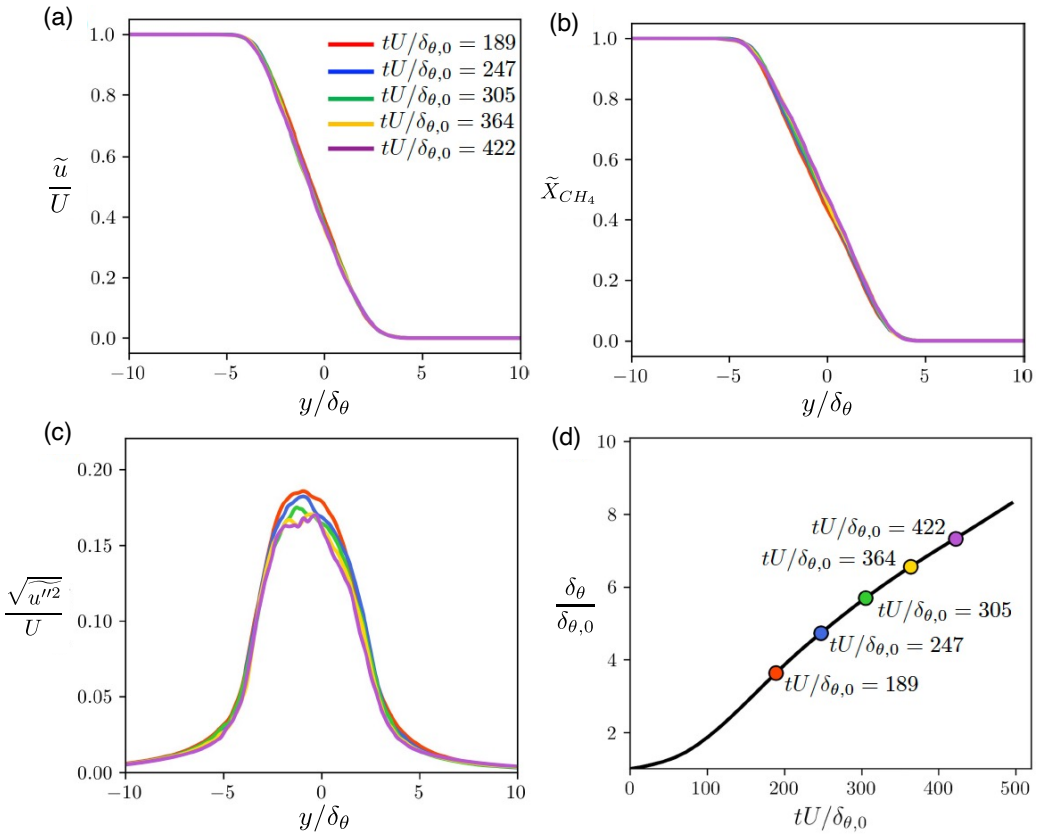

Figure 5: Dimensionless simulation results for a non-premixed turbulent shear layer in the absence of laser-energy deposition, including (a) mean streamwise velocity, (b) mean molar fraction of fuel, (c) streamwise Reynolds stress, and (d) momentum thickness.

and timing t_d of the laser-energy deposition are such that the interaction of kernel with the shear layer occurs within this quasi-linear growth period.

2.8. Discretization and computational grid

The HTR solver is based on a low-dissipation, sixth-order targeted essentially non-oscillatory (TENO) scheme in conjunction with a flux limiter on the convective term in Eq. (4), which acts locally to preserve positivity of mass fractions [47]. Time integration is performed with a third-order strong-

stability-preserving Runge-Kutta method. The simulation domain is discretized by a Cartesian mesh with $840 \times 1120 \times 560$ points in the x, y, and z directions, respectively, which amount to 527 million grid points. The grid spacing, $\Delta x = \Delta y = \Delta z = 14.3\,\mu$m, is uniform and corresponds to $1.7 \times \min(\eta^*)$, where η^* is the Kolmogorov length $\eta = (\overline{\nu}^3/\epsilon)^{1/4}$ at the representative end time. This resolution corresponds to $\delta_f/6.4$, where $\delta_f = 91\,\mu$m is the thickness of a stoichiometric CH_4/O_2 laminar premixed flame. As shown in Table 2, the domain size accommodates several momentum thicknesses and integral lengths. The latter are defined as $\ell_x = (\overline{u})^{-2} \int_{-\infty}^{+\infty} \overline{u(x,y,z,t)u(x+r,y,z,t)}dr$ for the x direction, and $\ell_z = (\overline{u})^{-2} \int_{-\infty}^{+\infty} \overline{u(x,y,z,t)u(x,y,z+r,t)}dr$ for the z direction.

2.9. Computation of ejecta-localized variables

To calculate representative values of flow variables in the ejecta, its lower edge is identified by the farthest extent of the coordinate y where the local temperature on the $\{x,z\}$ plane is higher than $2T_\infty = 600$ K. Denoting this coordinate by y_e, the ejecta temperature T_e and O molar fraction X_{Oe} are defined as the maximum of those variables in the region $y_e - 2R_2 \le y \le y_e + 2R_2$ over the entire ranges of x and z. The absolute values of the maximum flow velocity components u and v in the ejecta are defined in a similar manner. The ejecta velocity is computed as $U_e = -dy_e/dt$ and resembles the effective auto-advection speed of the vortex ring [28]. The time t_{in} for the ejecta to intercept the shear layer is defined as that when the maximum temperature in the spatial window $y_0 - \delta_\omega \le y \le y_0 + \delta_\omega$ exceeds $2T_\infty$, where y_0 is defined such that $\overline{u}_x(y_0) = U/2$. Instantaneous maximum values of temperature and O molar fraction in the shear layer are calculated within that same spatial window.

3. Results

This section begins with a description of the problem in the limit $y_L/L \to \infty$ corresponding to an isolated kernel in a stagnant O_2 environment. The analysis provides the ejecta velocity, temperature, and O molar fraction as a function of time, and serves to characterize the aerothermodynamics of the kernel unobstructed by the turbulent shear layer. Effects arising from the latter are subsequently studied for $y_L/L = O(1)$, with six simulation cases that exemplify scenarios leading to successful and unsuccessful ignition.

3.1. Early evolution of the kernel far away from the shear layer

The dynamics of the kernel are addressed here in the limit $y_L/L \to \infty$, in which the energy is deposited far away from the shear layer. The evolution of the kernel is summarized in Figs. 6 and 7. Specifically, in Fig 6 a qualitative time sequence of the meridian cross-section of the kernel depicts temperature and O molar fraction, along with the location of the shock and the initial kernel shape. Figure 7 gives time series of maximum temperature, O molar fraction, and velocity, focusing on early and late stages of energy deposition.

As shown in Fig. 7(a-c), the peak temperature exceeds 30,000 K upon depositing the energy at $t \sim t_d = 0.05\,\mu$s,

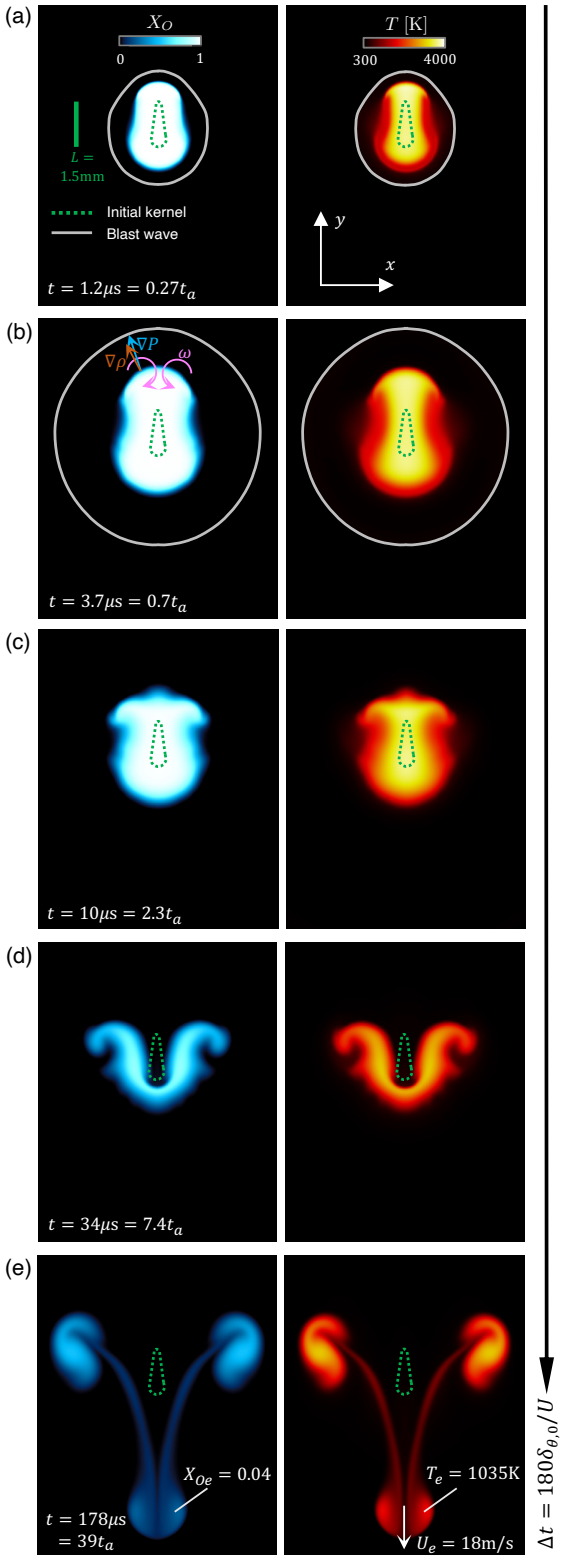

Figure 6: Time evolution of a meridian cross-section of the kernel resulting from laser deposition of energy in pure O_2 far away from the shear layer.

leading to near-complete dissociation of O_2 into O through the reaction $2O_2 \to 2O + O_2$. Note that incorporation of thermal radiation in Eq. (6) would decrease this peak temperature and shorten this first stage. Thereafter, the kernel expands due to the

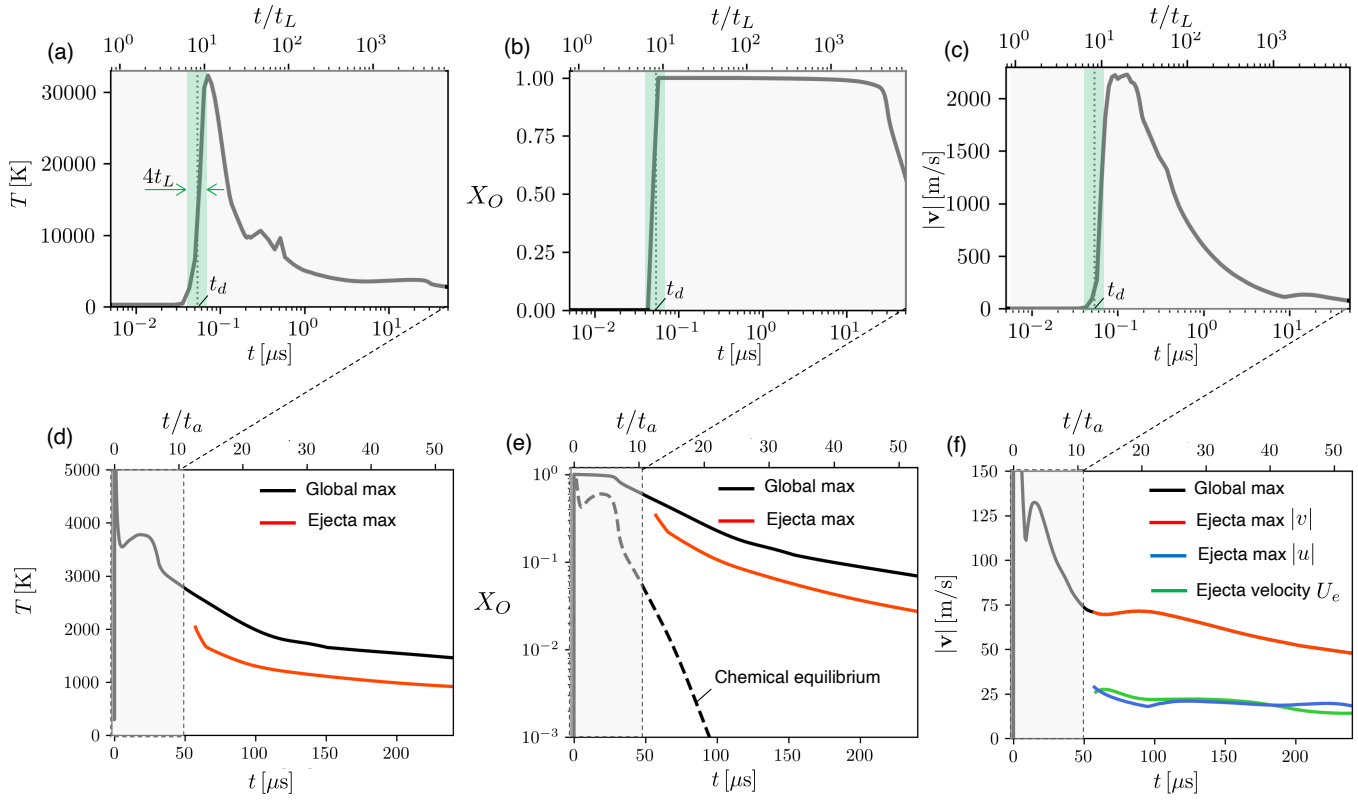

Figure 7: Time traces of maximum values of (a) temperature, (b) O molar fraction, and (c) velocity in the kernel resulting from laser deposition of energy in pure O_2 far away from the shear layer. Panels (d-f) are analogous but show longer time windows along with properties of the ejecta once is formed. The dashed lines and inset panel in (e) correspond to the molar fractions of atomic oxygen obtained assuming chemical equilibrium at the global maximum temperature (black dashed lines) and at the ejecta temperature (red dashed line). The laser pulse width is approximated by the green-colored region in panels (a-c). The maxima inside the ejecta denoted by the red and blue lines in panels (d-f) are plotted only after the ejecta has formed, corresponding to the time at which the vorticity has completely penetrated through the kernel core.

high post-deposition pressure, generating a blast wave and local gas velocities in excess of 2 km/s. After a time of approximately $100t_L$ has passed, roughly corresponding to the acoustic time $t_a = 4.5$ μs, the blast wave has propagated away to distances of order L from the kernel, the latter having cooled down to ten-fold lower temperatures. However, during this expansion, the temperature of the kernel remains much higher than the temperature behind the blast wave because of the fairly moderate Mach numbers of the latter, as observed in the temperature contours in Fig. 6(a,b). Concurrently with this expansion, the gas velocity decreases everywhere to subsonic values, as shown in Fig. 7(c). Also accompanying this expansion is a decrease in the concentration of atomic oxygen because of the prevailing effect of the recombination via $2O + O_2 \rightarrow 2O_2$. Nonetheless, the expansion is too fast for chemical equilibrium to settle, and therefore O is always found at super-equilibrium concentrations. In particular, O is typically found at molar fractions 10,000 times larger than those predicted by chemical equilibrium at the instantaneous ejecta temperature T_e.

After that first cooling phase, baroclinically generated vorticity distorts the rounded conical shape of the kernel. The time evolution of the temperature, O molar fraction, and velocity, provided in Fig. 7(d-e) for $t \gg t_a$, are now influenced by the mixing and stretching of the kernel. This process is visualized in Fig. 6(b-d) and has been characterized in early work [28]. Briefly, the ejecta is initiated by baroclinicity on the smaller (upper) lobe of the kernel during times of order t_a, while the blast wave is still nearby at distances of order L from the kernel. In the vicinity of the upper lobe, the pressure gradient is much more radially spread by the shock in a spherically-symmetric fashion than the more spatially-focused density gradient, the latter still tracing the high temperatures in the kernel instead, as sketched in Fig. 6(b). The sign and strength of the engendered vorticity in the upper lobe is such that it induces, over a long time of order $L/U_e \gg t_a$, a downward ejecta reminiscent of the one observed experimentally in Fig. 1. This creates two vortex rings: (a) An upper one that remains nearly-stationary at a mostly constant value of y but contains the largest amount of O and the highest temperature, and (b) a lower one at the tip of the ejecta moving downwards along the y axis at a velocity U_e. The resulting values of U_e in Fig. 7(e) are within the range 17 – 25 m/s.

As an example, at $t = 39t_a = 178$ μs shown in Fig. 6(e), which corresponds to 180 shear-layer time units $\delta_{\theta,0}/U$, the ejecta propagates at $U_e \simeq 18$ m/s and its edge is located at $y_e \simeq 4L$ away from the center of the initial kernel. Although the gas advects and cools, the recombination is sufficiently slow that the ejecta maintains a significant super-equilibrium concentration of O atoms. As indicated in Fig. 7(e), the peak mass fraction of O in the ejecta is approximately 4% at a peak tem-

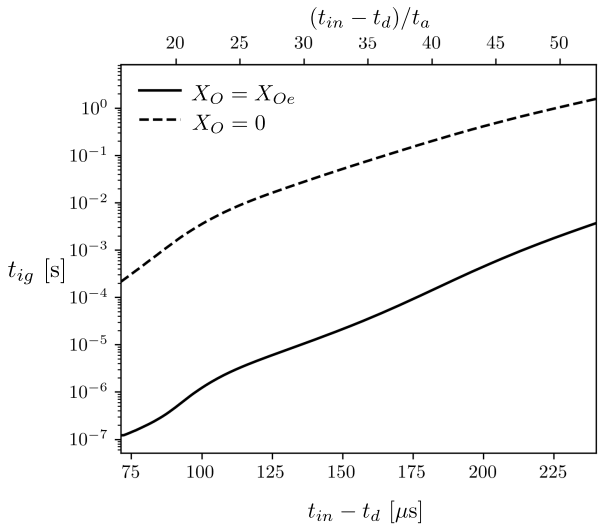

Figure 8: Homogeneous ignition time of a stochiometric CH_4/O_2 mixture if it were to encounter the local conditions in the ejecta as a function of the elapsed time at ejecta/shear-layer interception $t_{in} - t_d$, both in dimensional and acoustic-time units. The initial conditions correspond to the instantaneous ejecta temperature T_e and ejecta O molar fraction X_{Oe} (solid line) obtained from Fig. 7(d,e), along with a case assuming the same initial temperature but no initial presence of O atoms (dashed line).

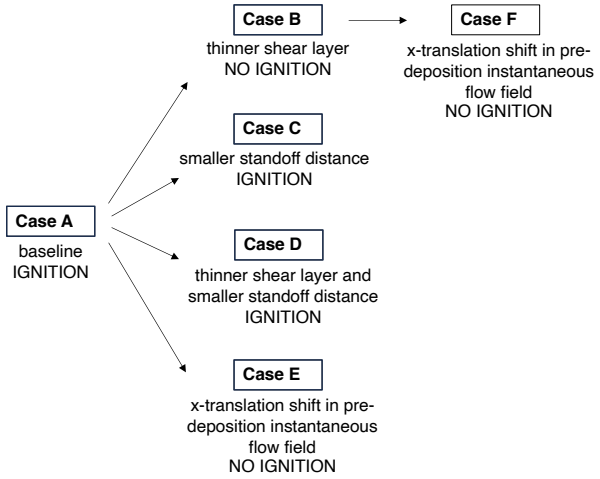

Figure 9: Summary of simulation cases and their outcomes.

perature of 1,035 K.

3.2. Interaction of the kernel with the turbulent shear layer

The remnant O atoms in the ejecta have a significant acceleration effect on the ignition time. This effect is quantified in Fig. 8 providing, as a function of the time elapsed at ejecta/shear-layer interception $t_{in} - t_d$, the homogeneous ignition time t_{ig} that a stochiometric CH_4/O_2 mixture would have if it were to encounter the temperature T_e and O molar-fraction X_{Oe} conditions in the ejecta. Both T_e and X_{Oe} evolve with the time elapsed since laser deposition in accordance with the red solid lines in Fig. 7(d,e). For instance, in the case of Fig. 6(e) at $t = 39t_a = 178\,\mu$s, a 4% of O in the ejecta at 1,035 K would lead to a homogeneous ignition time $t_{ig} \sim 0.1$ ms, which is 1,000 times shorter compared to that of a stoichiometric CH_4/O_2 mixture at the same temperature without O atoms. The acceleration effect of O atoms on the ignition of hydrocarbon fuels is well known from fundamental studies on supersonic combustion, contaminants in kinetic experiments, and plasma-assisted ignition [64–67]. In the current case, the O atoms accelerate radical chain reactions by attacking CH_4 via $CH_4 + O \rightarrow CH_3 + OH$, thereby promoting radical production and bypassing the slower initiation reaction $CH_4 + O_2 \rightarrow CH_3 + HO_2$.

Figure 9 provides the rationale for the six cases A-F simulated in this study, which are summarized also in Table 3 and visualized with instantaneous density contours in Fig. 10 (see also Movies A-F in the Supplementary Material). In all cases, the laser energy is deposited within the kernel geometry described in Fig. 4 centered at a minimum of approximately $10\delta_\theta$ units away from the shear-layer centerline, where the mean molar fraction of CH_4 is negligible, as shown in Fig. 5(b).

Case A corresponds to a baseline configuration in Fig. 10(a) that leads to ignition. Determination of ignition is based here on the development of a clear thermal runaway accompanied

	Case A	Case B	Case C	Case D	Case E	Case F
Laser-deposition time in shear-layer units, $t_d U/\delta_{\theta,0}$	306	102	306	102	306	102
Laser focal position, y_L/L	2.67	2.67	2.00	2.00	2.67	2.67
Shear-layer shift in integral-length units, $x_s/\ell_x(t_d)$	0	0	0	0	16.7	12.5
Elapsed time at ejecta/shear-layer interception in acoustic-time units, $(t_{in} - t_d)/t_a$	27.5	32.2	15.8	19.9	26.3	31.1
Total elapsed time at ejecta/shear-layer interception in shear-layer time units, $t_{in}U/\delta_{\theta,0}$	430	247	377	192	424	242
Vorticity thickness at ejecta/shear-layer interception in kernel length units, $\delta_\omega(t_{in})/L$	1.18	0.86	1.16	0.68	1.26	0.84
T_e at ejecta/shear-layer interception [K]	1152	1091	1242	1088	1137	1092
X_{Oe} at ejecta/shear-layer interception	0.09	0.06	0.25	0.19	0.09	0.07
Ignition Damköhler number at ejecta/shear-layer interception, Da_{in}	1.75	0.27	40.7	6.40	2.50	0.36
Outcome	IGNITION	NO IGNITION	IGNITION	IGNITION	NO IGNITION	NO IGNITION

Table 3: Quantitative case matrix for the simulations performed in this study.

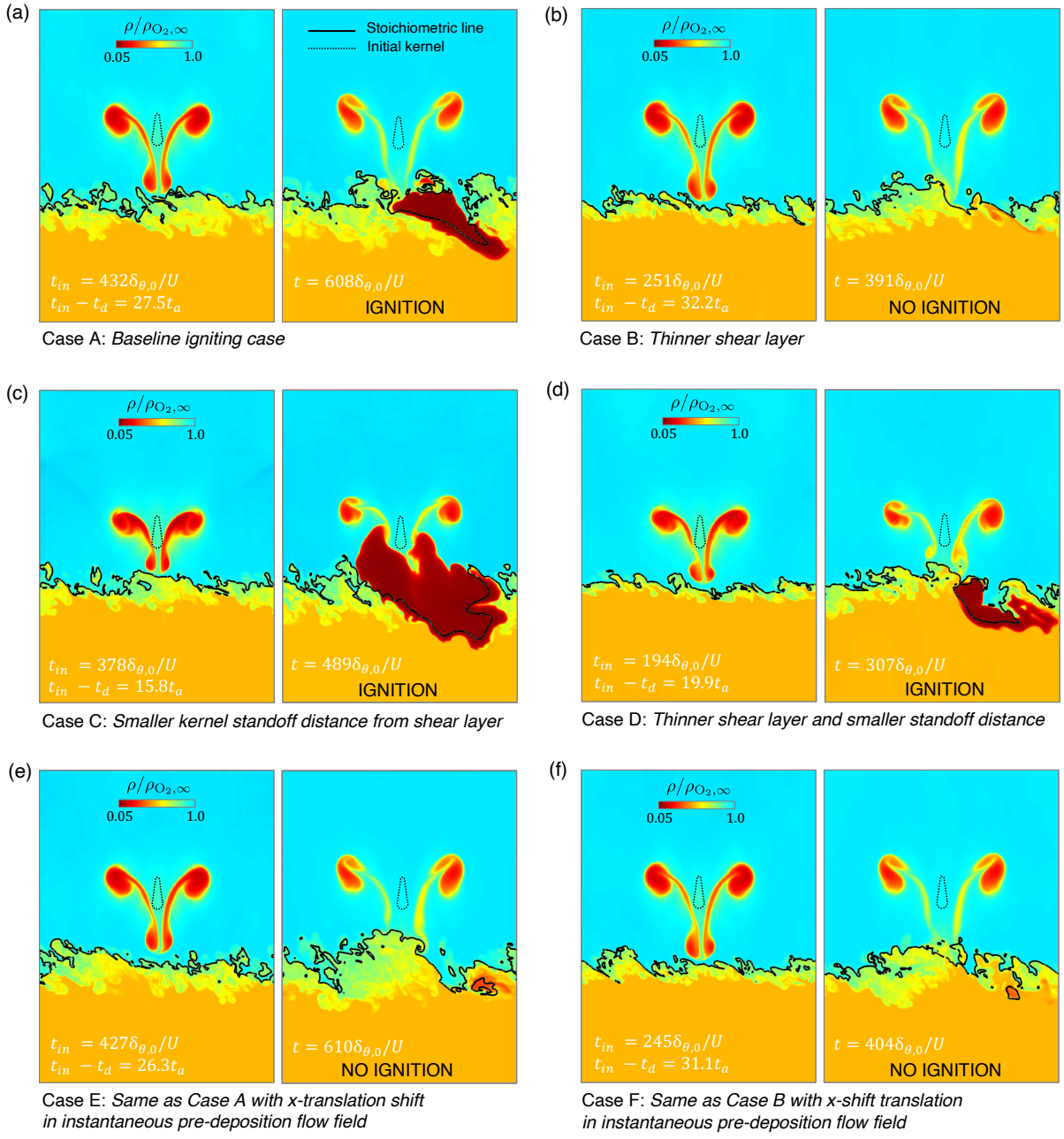

Figure 10: Instantaneous density contours on the $z = 0$ plane for cases A-F in Table 3 (see also Movies A-F in the Supplementary Material). For each case, the left panel represents instantaneous conditions at ejecta/shear-layer interception, whereas the right panel shows instantaneous conditions at a later time sufficiently long to evaluate whether ignition occurred.

with maximum temperatures close to the adiabatic flame temperature, as observed in Fig. 11(a,c). Note that there is a limited spatiotemporal window of $L_x/2 \simeq 6$ mm and $L_x/(2U) \simeq 120\,\mu$s for post-interception assessment of successful or unsuccessful ignition in this configuration, since the simulation must be terminated before the combustion gases reach the downstream boundary of the computational domain to avoid an unrealistic recirculation because of periodicity. According to the ignition-delay estimate provided by the solid line in Fig. 8, this available window should be sufficient to discern successful ignition up to ejecta/shear-layer interception elapsed times $t_{in} - t_d \sim 45t_a$, which is a condition verified by all cases in Table 3.

Case B reproduces the same configuration as case A but the laser energy is deposited earlier during the development of the shear layer. The comparatively smaller value of δ_ω at interception leads to ignition failure, with the hot ejecta being washed away by turbulence in the shear layer, as shown in Fig. 10(b). Case C has also the same configuration as case A but considers a smaller standoff distance y_L, so that the laser is focused closer to the shear layer, thereby leading to higher T_e and X_{Oe}. This results in ignition, as shown in Fig. 10(c). In case D, the ignition-favorable effect of decreasing the kernel standoff dis-

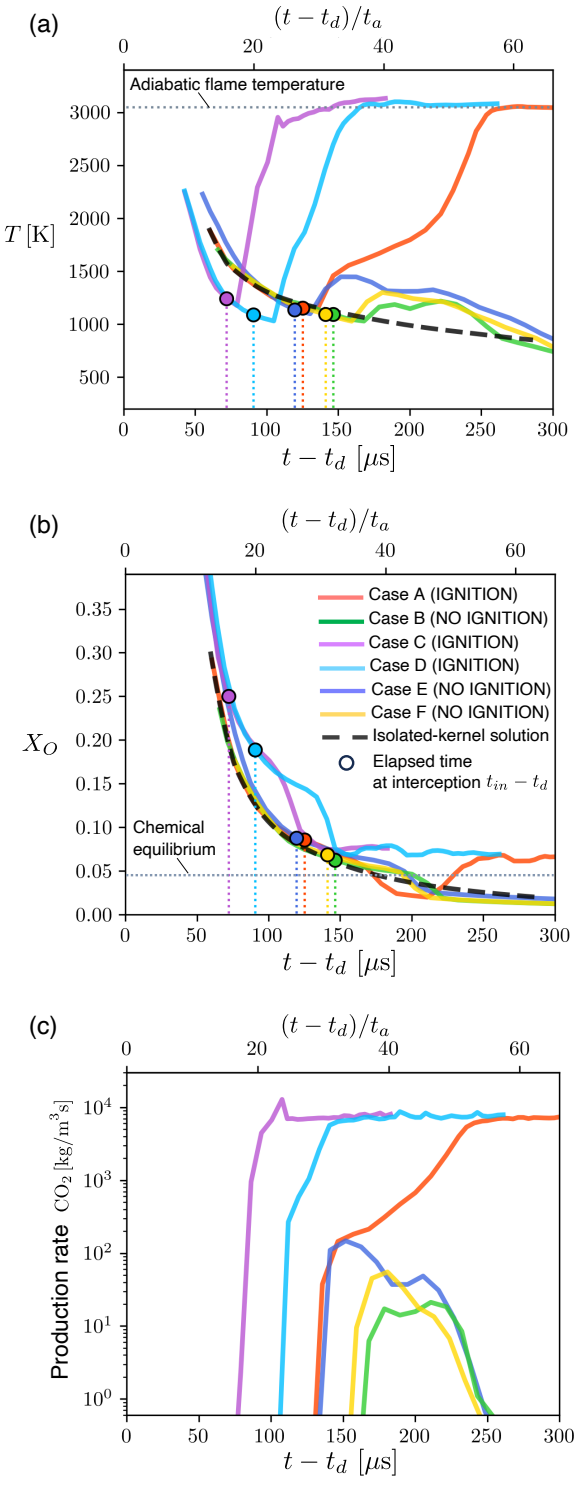

Figure 11: Time traces of (a) maximum temperature and (b) maximum O molar fraction near the ejecta/shear-layer interception zone, along with (c) global maximum CO_2 mass production rate in the flow field. The dotted horizontal lines in panels (a) and (b) represents the adiabatic flame temperature (3, 049 K) and burnt-gas chemical-equilibrium molar fraction of atomic oxygen (0.045) for a stoichiometric laminar premixed flame at an unburnt temperature of 300 K.

tance prevails over the ignition-unfavorable effect of advancing laser-energy deposition in time, as observed Fig. 10(d). Translations of the pre-deposition flow field in the periodic x direction are performed in cases E and F to probe sensitivity of ignition to the instantaneous fluctuations. Specifically, as shown in Fig. 10(e), the translation in case E suppresses the ignition observed in the baseline case A. In contrast, the translation in case F, shown in Fig. 10(f), is not capable of overturning the ignition failure observed in the reference case B.

Closer examination of the conditions at interception in Table 3 and Fig. 11 helps to rationalize these results. Because of cooling and O−atom recombination in the ejecta, the homogeneous ignition time in Fig. 8 increases exponentially with the elapsed time at interception approximately as

$$t_{ig} \sim C_2 \exp[(t_{in} - t_d)/C_3], \tag{15}$$

with $C_2 \simeq 1823\ \mu$s and $C_3 \simeq 16\ \mu$s. As a result, small values of $t_{in} - t_d$ are desirable for ignition. Since $t_{in} - t_d \sim (y_L - \delta_\omega)/U_e$, early interception can be achieved in two different ways for a given value of E: (a) Depositing the laser energy when the shear layer is relatively thick (i.e., large δ_ω), or (b) placing the laser focus close to the shear-layer centerline (i.e., small y_L).

Case A involves interception when the shear layer is relatively thick. As shown in Fig. 11, after a time of approximately $200\delta_{\theta,0}/U$ has passed since laser-energy deposition, the maximum temperature and O molar fraction in the shear layer are very close to those in the burnt gas of a stoichiometric laminar premixed flame propagating at P_∞ and T_∞. The complete sequence of ignition for case A is provided in Fig. 12 (see also Movie A in the Supplementary Material), including: (a) The baroclinically generated vorticity on the upper kernel lobe, (b) the evolution of the blast wave, (c) its refraction across the shear layer, (d) the pairing of the leeward vortex of the ejecta with the shear layer, along with (e) the early ignition spot and (f) the subsequent flame propagation. In case A, as in all other cases treated here, the blast wave is too weak to ignite the shear layer. However, there could be configurations with larger E or smaller y_L in which the blast wave may ignite the shear layer [68].

The igniting cases C and D involve a decrease in y_L with respect to the baseline, leading to the smallest values of $t_{in} - t_d$ and relatively high content of O atoms in the ejecta. Specifically, as shown in Fig. 11(a,b), T_e and X_{Oe} are, respectively, significantly smaller and larger for these cases than those for an isolated kernel. In contrast, near interception, the ejecta in case A displays values much closer to the isolated-kernel solution. This can be understood by noticing that the blast wave partly reflects from the CH_4 stream as an expansion wave that cools the ejecta and further freezes its chemical composition. This effect becomes increasingly more important as y_L decreases and therefore is clearly observable in cases C and D.

To quantitatively explain these observations, an ignition Damköhler number at ejecta/shear-layer interception, Da_{in}, can be defined as the ratio of the large-scale eddy turnover time δ_θ/U and the ignition time t_{ig}, namely

$$Da_{in} = \frac{\delta_\theta}{U t_{ig}} \sim \frac{C_1 t_{in}}{C_2 \exp[(t_{in} - t_d)/C_3]}, \tag{16}$$

where use has been made of Eqs. (14) and (15). Figure 13 shows that large values $Da_{in} \gg 1$ correspond to laser-energy

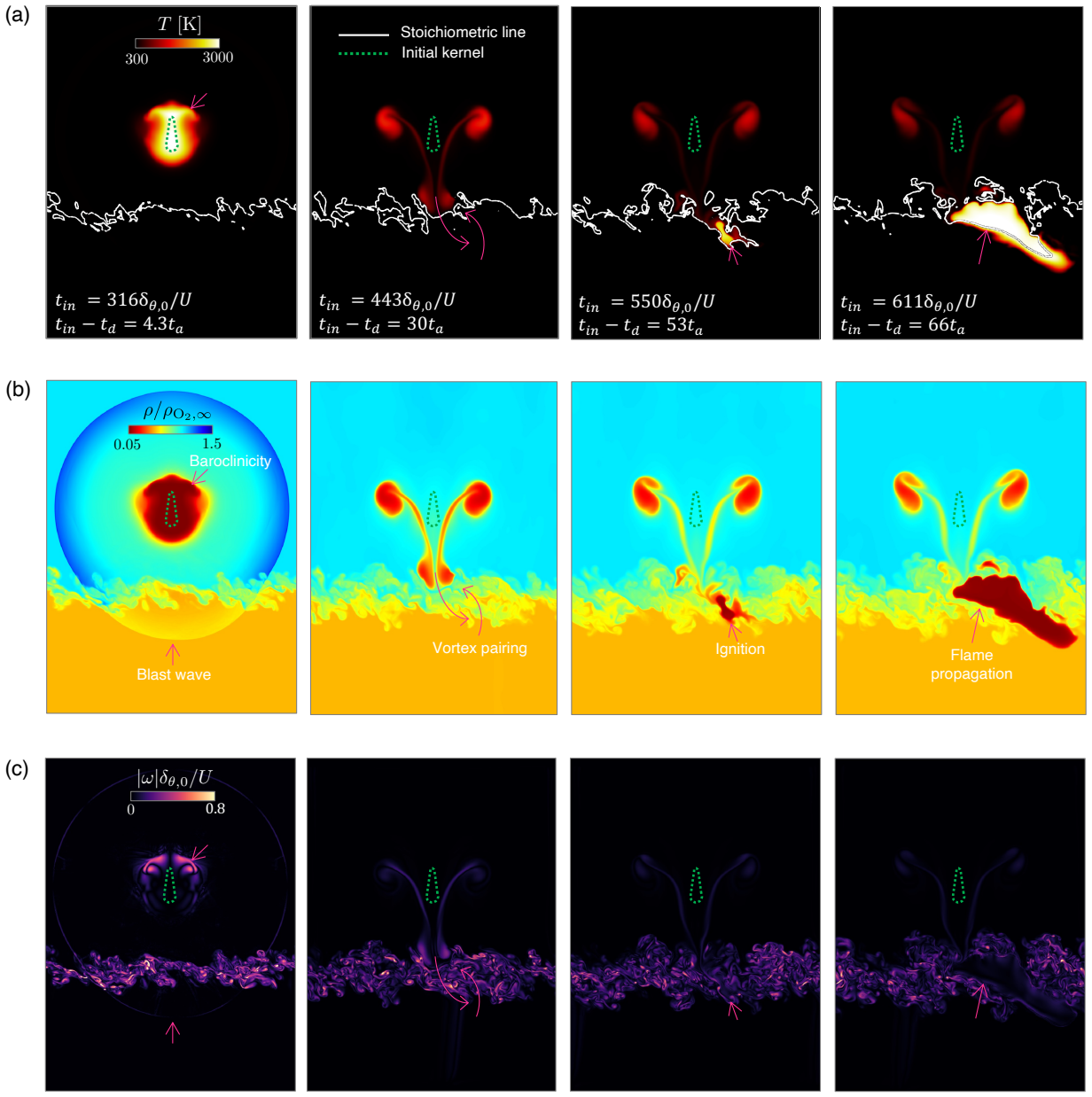

Figure 12: Instantaneous (a) temperature, (b) density, and (c) vorticity contours on the $z = 0$ plane for case A in Table 3 (see also Movie A in the Suppl. Mat.).

deposition at late times (i.e., large t_d, or equivalently, small characteristic strain rate U/δ_θ), followed shortly after by the ejecta/shear-layer interception (i.e., small $t_{in} - t_d$, or equivalently, small y_L and large δ_w). As listed in Table 3, the igniting cases C and D are characterized by large values of Da_{in}, whereas the other cases have either $Da_{in} \sim 1$ or $Da_{in} \ll 1$, the latter pertaining to the non-igniting cases B and F.

To refine the analysis, the large-scale eddy turnover time δ_θ/U in Eq. (16) could be replaced with one based on the mean magnitude of local strain rate, such as $1/\overline{(\boldsymbol{S}:\boldsymbol{S})}^{1/2} \sim \eta^2/\overline{\nu}$, accounting for the large strain rate in the microscales. However, because of the moderate Re_θ and the proximity of the stoichiometric line to the oxidizer edge of the shear layer, where the turbulent fluctuations are much weaker, it can be shown that the resulting values of Da_{in} would differ only by a factor of order unity from those in Fig. 13. Similar conclusions apply when the inverse of the scalar dissipation rate is used instead.

The above results suggest that Da_{in} is a useful parameter to predict ignition in this configuration. However, and rightly so, the description of the results requires additional considerations for cases with near-unity Da_{in}. Specifically, ignition in those cases also depends on instantaneous local flow conditions near the ejecta/shear-layer interception zone. This can be easily shown by comparing cases A and E. A non-igniting solution is obtained in case E by translating the instantaneous pre-deposition flow field of case A in the x direction by a sufficiently large distance that warrants decorrelation of the fluctuations while preserving all turbulence statistics, as done in

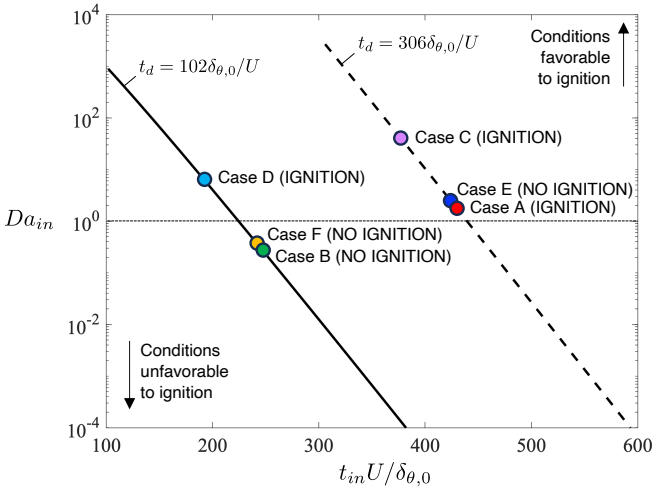

Figure 13: Ignition Damköhler number at ejecta/shear-layer interception Da_{in} as a function of the elapsed time t_{in} for two laser-energy deposition times t_d.

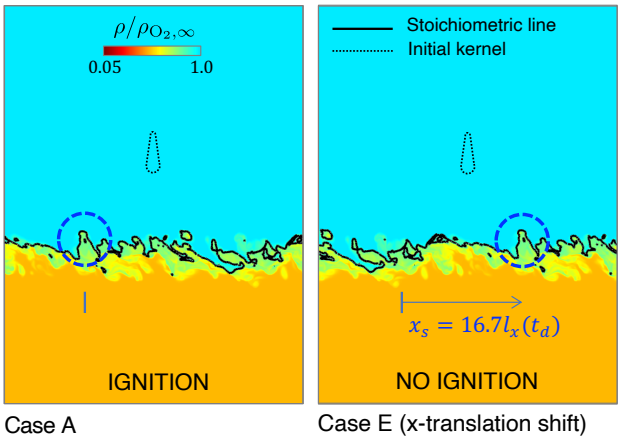

Figure 14: Instantaneous pre-deposition flow field at $t - t_d = -5t_L$ for cases A (left panel) and E (right panel) in Table 3. For visual clarity, the same flow feature is circled before and after the x-translation shift of the flow field.

Fig. 14 (see also Movie E in the Supplementary Material). This occurs despite the fact that cases A and E both follow similar time histories before interception, as shown in Fig. 11, and have comparable near-unity values of Da_{in}, as indicated in Table 3 and Fig. 13. However, a similar translation in case F does not change the outcome of the reference case B, whose value of Da_{in} is much smaller than case A. These observations suggest the potential effect of local intermittency near the oxidizer edge of the shear layer as another key factor that influences ignition for near-unity values of Da_{in}.

3.3. Additional effects of the orientation, focus location, and propagation direction of the laser beam

Whereas in all cases treated above the laser has been assumed to propagate upwards along the y direction and is focused on the oxidizer side, the solution of problem may be sensitive to all those aspects, as sketched in Fig. 15. The cartoons provided there are exclusively based on physical intuition and the fact that some configurations such as those in Fig. 15(c,h) cannot lead to effective vortex pairing because of destructive interference between the mean vorticity of the turbulent shear layer and that of the ejecta. Other configurations such as those in Fig. 15(b,f) are also ineffective for relying on the opposite quasi-stationary vortex ring of the kernel for ignition. Note that focusing the laser on the fuel side, as in Fig. 15(b,e,g,h), would lead to production of H and CH_3 radicals by photodissociation of CH_4, and therefore to acceleration of ignition. These additional aspects are deferred to future work.

4. Conclusions

In this study, DNS have been employed to address the laser-induced indirect ignition of temporally-evolving non-premixed turbulent subsonic shear layers separating two gaseous streams of CH_4 and O_2. Consistent with previous experiments [13], indirect ignition was observed by focusing the laser on the O_2 environment, despite the fact that the local composition there was far beyond the lean flammability limit at all times. This indirect ignition mode developed after relatively long times compared with the characteristic acoustic time, when the eddies on the oxidizer edge of the turbulent shear layer are intercepted by a baroclinically generated ejecta emanating from the kernel, which contains dissociated oxygen at moderate temperatures. The success of indirect ignition was characterized by an ignition Damköhler number that revealed ignition-favorable conditions involving short standoff distances of the kernel from the shear-layer centerline, along with relatively thick shear layers or short ejecta/shear-layer interception times elapsed since laser-energy deposition. For near-unity ignition Damköhler numbers, a simple translation of the instantaneous pre-deposition flow field rendered different ignition outcomes, thereby indicating a sensitivity of the ignition phenomena to the local turbulent fluctuations near the ejecta/shear-layer interception zone.

The considerations above suggest that the probability distribution function for laser-induced ignition may be spatially broader than ideally predicted with concentrated or spherico-symmetric kernel models, in that the laser may be focused on zones exceedingly rich in oxidizer and still induce ignition. In practice, this finding decreases the sensitivity of ignition to the spatial location of the laser focal region and therefore reduces the risk of engine re-start failure.

A number of simplifications have been made in this study with the goal of focusing on the aerothermodynamics of the ignition kernel and its interaction with the turbulent shear layer. Perhaps the most prominent aspects worth revisiting in future studies are the incorporation of the laser-beam propagation physics and kernel plasmadynamics, along with the multiphase character of propellant flows in rocket engines. Whereas the refraction of the laser beam through the shear layer and its early electrodynamic coupling with the ensuing plasma have been neglected here, simulations including these effects may lead to further understanding of time histories of excited and radical species in the ejecta during the cooling phase. Similarly, the preponderant use of cryogenic propellants in rocket engines, along with the low pressures typically reigning in the combustor

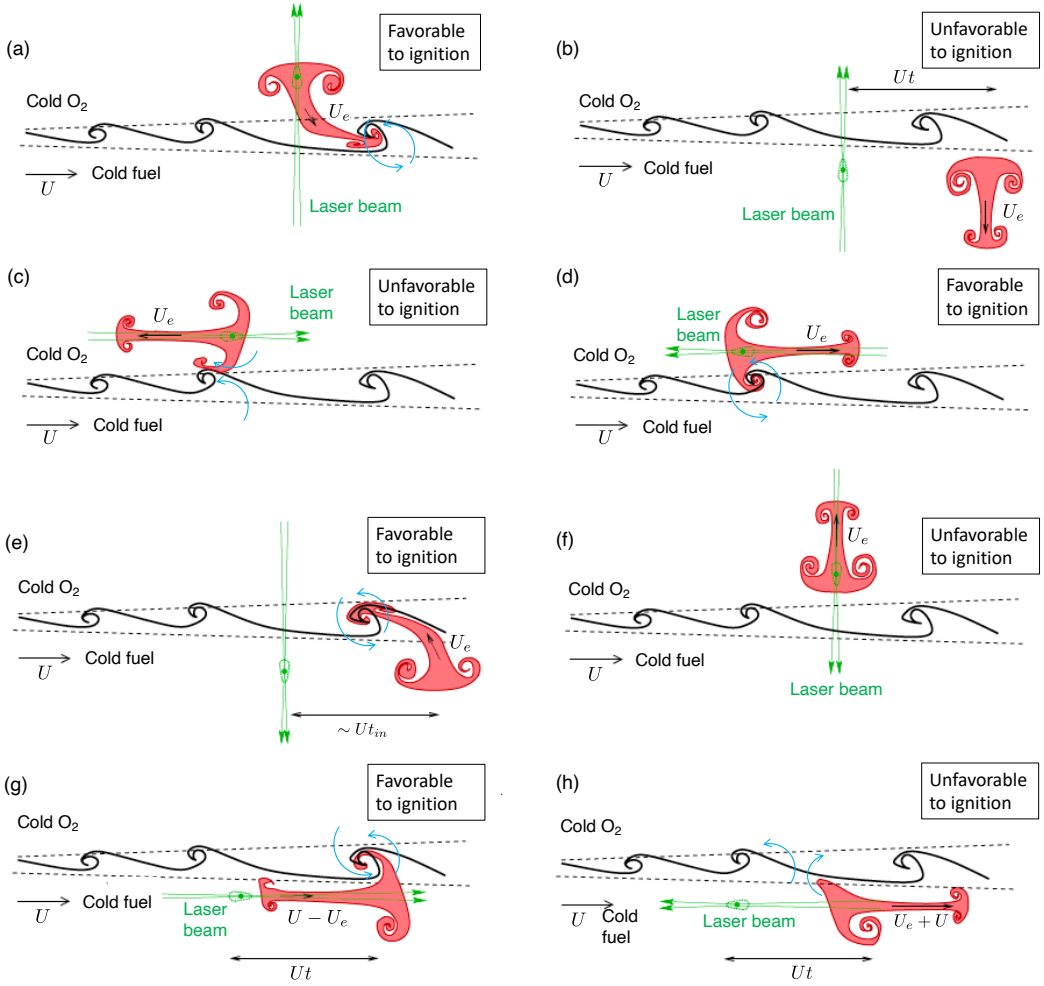

Figure 15: Favorable and unfavorable effects of the laser-beam orientation, focus location, and propagation direction on indirect ignition of the turbulent shear layer. These schematics are only grounded on basic physical aspects of the ejecta and vorticity field, and remain to be substantiated by simulations in future work.

upon engine ignition or restart at high altitudes, require consideration of laser propagation through sprays, interaction of the kernel with droplets, along with propellant flashing.

Acknowledgments

This investigation was funded by the US Department of Energy's National Nuclear Security Administration (NNSA) via the Stanford PSAAP-III Center for prediction of laser-induced ignition of rocket engines, Grant # DE-NA0003968.

References

[1] L.C. Liou. Laser ignition in liquid rocket engines. In 30th Joint Propulsion Conference and Exhibit, 1994.

[2] K. Hasegawa, K. Kusaka, A. Kumakawa, M. Sato, M. Tadano, and H. Takahashi. Laser ignition characteristics of GOX/GH2 and GOX/GCH4 propellants. In 39th Joint Propulsion Conference and Exhibit, 2003.

[3] G. Lacaze, B. Cuenot, T. Poinsot, and M. Oschwald. Large eddy simulation of laser ignition and compressible reacting flow in a rocket-like configuration. *Combust. Flame* 156, 1166-1180, 2009.

[4] C. Pauly, J. Sender, and M. Oschwald. Ignition of a gaseous methane/oxygen coaxial jet. *Prog. Propulsion Phys.* 1, 155-170, 2009.

[5] C. Manfletti and M. Börner. Ignition overpressure in laser ignited reaction and control thrusters. In AIAA Propulsion and Energy Forum, 2014.

[6] C. Manfletti. Laser ignition of an experimental cryogenic reaction and control thruster: pre-ignition conditions. *J. Propulsion and Power*, 30: 925-933, 2014.

[7] C. Manfletti. Laser ignition of an experimental cryogenic reaction and control thruster: ignition energies. *J. Propulsion and Power*, 30:952-961, 2014.

[8] M. Börner, C. Manfletti, G. Kroupa, and M. Oschwald. Laser ignition of a multi-injector research combustion chamber under high-altitude conditions. In 7th European Conference for Aeronautics and Space Sciences (EUCASS), 2017.

[9] G. Kroupa and M. Börner. A miniaturized high-energy laser for ignition of rocket engines. In International Conference on Space Optics (ICSO), 2018.

[10] M. Börner, C. Manfletti, J. Hardi, D. Suslov, M. Oschwald, and G. Kroupa. Comparison of laser ignition and torch ignition in a subscale rocket combustor. In AIAA Propulsion and Energy Forum, 2018.

[11] G. Gargiulo, P. P. Ciottoli, E. Martelli, R. Malpica-Galassi, and M. Valorani. Numerical analysis of laser-pulse transient ignition of oxygen/methane mixtures in rocket-like combustion chambers. *Acta Astronautica*, 159:136-155, 2019.

[12] J. Wang, M. Di Renzo, C. Williams, J. Urzay, and G. Iaccarino. Progress on laser ignition simulations of a CH4/O2 subscale rocket combustor using a multi-GPU task-based solver. *Annual Research Briefs*, Center for Turbulence Research, Stanford University, pp. 129-142, 2021.

[13] R. Strelau, M. Frederick, W. C. Senior, R. Gejji, and C.D. Slabaugh. Modes of laser spark ignition of a model rocket combustor. In *AIAA Scitech*, Paper #2023-2377, 2023.

[14] N. G. Glumac and G. S. Elliott, The effect of ambient pressure on laser-

induced plasmas in air. *Optics Lasers Eng.*, 45:27–35, 2007.
[15] J. M. Wang and J. B. Freund. Hydrodynamic ejectas by dual-pulse laser-induced breakdowns. *AIAA J.* 58, 3544–3551, 2020.
[16] D. Bradley, C. G. W. Sheppard, I. M. Suardjaja, and R. Woolley. Fundamentals of high-energy spark ignition with lasers. *Comb. Flame* 138, 55-77, 2004.
[17] A. Alberti, A. Munafò, M. Koll, M. Nishihara, C. Pantano, J. B. Freund, G. Elliott, and M. Panesi. Laser-induced non-equilibrium plasma kernel dynamics. *J. Phys. D: Applied Phys.* 53, 025201, 2019.
[18] A. Munafò, A. Alberti, C. Pantano, J. B. Freund, and M. Panesi. A computational model for nanosecond pulse laser-plasma interactions. *J. Comp. Phys.* 406, 109190, 2020.
[19] J.M. Wang, M. Panesi, and J. B. Freund. 2021. Thermal effects mediating the flow induced by laser-induced optical breakdown. *Phys. Rev. Fluids* 6, 63403, 2004.
[20] T. X. Phuoc. Laser-induced spark ignition fundamental and applications. *Optics Lasers Eng.* 44:351-397, 2006.
[21] M. H. Morsy and S. H. Chung. Numerical simulation of front lobe formation in laser-induced spark ignition of ch4/air mixtures. *Proc. Combust. Inst.* 29:1613–1619, 2002
[22] R. Kandala and G. V. Candler. Numerical studies of laser-induced energy deposition for supersonic flow control. *AIAA J.* 42:2266–2275, 2004.
[23] S. Ghosh and K. Mahesh. DNS of the thermal effects of laser energy deposition in isotropic turbulence. *J. Fluid Mech.* 654: 387–416, 2010.
[24] S. Brieschenk, S. O'Byrne, and H. Kleine. Visualization of jet development in laser-induced plasmas. *Optics Lett.* 38: 664–666, 2013.
[25] S. S. Harilal, B. E. Brumfield, and M. C. Phillips. Lifecycle of laser-produced air sparks. *Phys. Plasmas* 22: 063301, 2015.
[26] B. An, Z. Wang, L. Yang, G. Wu, J. Zhu, and X. Li. Experimental investigation of the shock loss and temporal evolution of hot plume resulting from dual-pulse laser-induced breakdown in quiescent air. *J. App. Phys.* 122: 193301, 2017.
[27] L. Wermer and S.-K. Im, Plasma and flow induced by single- and dual-pulse laser-induced breakdown in stationary air. *Plasma Sources Sci. & Tech.* 28: 065004, 2019.
[28] J. M. Wang, D. A. Buchta and J. B. Freund. Hydrodynamic ejecta by laser-induced optical breakdown. *J. Fluid Mech.* 888: A16, 2020
[29] V. Kurdyumov, A.L. Sánchez, and A. Liñán. Heat propagation from a concentrated external energy source in a gas. *J. Fluid Mech.*, 491:379-410, 2003.
[30] V. Kurdyumov, J. Blasco, A.L. Sánchez, and A. Liñán. On the calculation of the minimum ignition energy. *Comb. Flame.*, 136:394-397, 2004.
[31] D.R. Ballal and A. Lefebvre. Ignition and flame quenching in flowing gaseous mixtures. *Proc. Royal. Soc. London A* 357:163–181, 1977.
[32] P. D. Ronney, Laser versus conventional ignition of flames. *Optical Eng.* 33:–522, 1994.
[33] E. Mastorakos. Ignition of turbulent non-premixed flames. *Prog. Ener. Comb. Sci.* 35:57–97, 2009.
[34] S. Jo and J.P. Gore. Laser ignition energy for turbulent premixed hydrogen air jets. 111767, 2022.
[35] L. Esclapez, E. Riber, and B. Cuenot. Ignition probability of a partially premixed burner using LES. *Proc. Combust. Inst.* 35:3133-3141, 2015.
[36] H.A. Uranakara, S. Chaudhuri, and K.N. Lakshmisha. On the extinction of igniting kernels in near-isotropic turbulence. *Proc. Combust. Inst.* 36: 1793-1800, 2017.
[37] J. Marrero-Santiago, F. Collin-Bastiani, E. Riber, G. Cabot, B. Cuenot, and B. Renou. On the mechanisms of flame kernel extinction or survival during aeronautical ignition sequences: Experimental and numerical analysis. *Combust. Flame* 222: 70–84, 2020.
[38] A. Eyssartier, B. Cuenot, L.Y. Gicquel, and T. Poinsot. A statistical model to predict ignition probability. *Combust. Flame* 160:1191-1207, 2013.
[39] L. Esclapez, F. Collin-Bastiani, E. Riber, and B. Cuenot. A statistical model to predict ignition probability. *Combust. Flame* 225:180-195, 2021.
[40] P.M. de Oliveira. *Ignition and propagation mechanisms of spray flames.* PhD Thesis, University of Cambridge, 2019.
[41] P.M. de Oliveira, M.P. Sitte, M. Zedda, A. Giusti, and E. Mastorakos. Low-order modeling of high-altitude relight of jet engine combustors. *Int. J. Spray Combust. Dyn.* 13:20-30, 2021.
[42] Y.B. Zel'dovich and Y.P. Raizer. *Physics of shock waves and high-temperature hydrodynamic phenomena*. Dover, 2002.
[43] J. Capecelatro, D. J. Bodony, and J. B. Freund. Adjoint-based sensitivity and ignition threshold mapping in a turbulent mixing layer. *Combust. Theory Model.* 23, 147–179, 2019.
[44] Y. Ju and W. Sun. Plasma assisted combustion: Dynamics and chemistry. *Prog. Ener. Combust. Sci.* 48:21-83, 2015.
[45] Y.P. Raizer. Breakdown and heating of gases under the influence of a laser beam. *Soviet Physics Uspekhi* 8:650-671, 1966.
[46] J. M. Wang, J. F. MacArt, and J. B. Freund. Flow dynamics of laser-induced breakdown at a fuel–oxidizer interface and its effect on ignition. *Combust. Flame* 229, 111375, 2021.
[47] M. Di Renzo, L. Fu, and J. Urzay. HTR solver: An open-source exascale-oriented task-based multi-gpu high-order code for hypersonic aerothermodynamics. *Comput. Phys. Commun.* 255, 107262, 2020.
[48] C.F. Curtiss and J.O. Hirschfelder. Transport properties of multicomponent gas mixtures. *J. Phys. Chem.* 17, 550-555, 1949.
[49] A. Ern and V. Giovangigli. Multicomponent transport algorithms. Lecture Notes in Physics Monographs, vol. 24. Springer, Berlin,1994.
[50] C. R. Wilke. A viscosity equation for gas mixtures. *J. Chem. Phys.* 18, 517–519, 1950.
[51] S. Mathur, P. K. Tondon, and S. C. Saxena. Thermal conductivity of binary, ternary and quaternary mixtures of rare gases. *Molecular Phys.* 12, 569–579, 1967.
[52] R. J. Kee, M. E. Coltrin, and P. Glarborg. *Chemically reacting flow: theory and practice.* Wiley & Sons, 2005.
[53] J. O. Hirschfelder, C. F. Curtiss, and R. B. Bird. *Molecular theory of gases and liquids*. Wiley & Sons, 1967.
[54] Y. Zhang, W. Dong, L. Vandewalle, R. Xu, G. P. Smith, and H. Wang. *Foundational Fuel Chemistry Model Version 2.0 (FFCM-2),* 2023. URL: https://web.stanford.edu/group/haiwanglab/FFCM2.
[55] R. Xu, S.S. Dammati, X. Shi, E.S. Genter, Z. Jozefik, M.E. Harvazinski, T. Lu, A. Poludnenko, V. Sankaran, A.R. Kerstein, and H. Wang. Modeling of high-speed methane-air turbulent combustion - Part II: Reduced methane oxidation chemistry. *Combust. Flame.* (under review), 2023.
[56] B. J. McBride, S. Gordon, and M. A. Reno. Coefficients for calculating thermodynamic and transport properties of individual species. NASA TM-4513, 1993.
[57] B.J. McBride, M. J. Zehe, and S. Gordon. NASA Glenn coefficients for calculating thermodynamic properties of individual species. NASA/TP?2002-211556, 2002.
[58] J.M. Wang. *Ignition and hydrodynamic ejectas by laser-induced breakdown.* PhD Thesis, University of Illinois Urbana Champaign, 2020.
[59] S. B. Pope. *Turbulent flows*. Cambridge University Press, 2010.
[60] T. J. Poinsot and S. K. Lele. Boundary conditions for direct simulations of compressible viscous flows. *J. Comput. Phys.* 101, 104–129, 1992.
[61] N. Okong'o and J. Bellan. Consistent boundary conditions for multicomponent real gas mixtures based on characteristic waves. *J. Comput. Phys.* 176, 330–334, 2002.
[62] C. Pantano and S. Sarkar. A study of compressibility effects in the high-speed turbulent shear layer using direct simulation. *J. Fluid Mech.* 451, 329?371, 2002.
[63] J. O'Brien, J. Urzay, M. Ihme, P. Moin, and A. Saghafian. Subgrid-scale backscatter in reacting and inert supersonic hydrogen-air turbulent mixing layers. *J. Fluid Mech.* 743, 554?584, 2014.
[64] I. Da Riva, A.Liñán, E. Fraga, and J.L. Urrutia. Diffusion flames and supersonic combustion. Technical Report, Instituto Nacional de Técnicas Aerospaciales Esteban Terradas, 1966.
[65] J. Urzay, N. Kseib, D.F Davidson, G. Iaccarino, and R.K. Hanson. Uncertainty-quantification analysis of the effects of residual impurities on hydrogen/oxygen ignition in shock tubes. *Combust. Flame* 161, 1-15, 2014.
[66] M.A. Boumehdi, S.A. Stepanyan, P. Desgroux, G. Vanhove, and S.M. Starikovskaia. Ignition of methane-and n-butane-containing mixtures at high pressures by pulsed nanosecond discharge. *Combust. Flame* 162, 1336-1349, 2015.
[67] L. Cheng, N. Barleon, B. Cuenot, O.Vermorel, and A. Bourdon. Plasma assisted combustion of methane-air mixtures: Validation and reduction. *Combust. Flame* 240, 111990, 2022.
[68] C. Huete, A.L. Sánchez, F.A. Williams, and J. Urzay. Diffusion-flame ignition by shock-wave impingement on supersonic mixing layers. *J. Fluid Mech.* 784, 74-108, 2015.

Laser-induced indirect ignition of non-premixed turbulent shear layers
Supplementary Material

Jonathan Wang[1], Mario Di Renzo[1], Gianluca Iaccarino[1,2], Hai Wang[2] and Javier Urzay[3]

[1] *Center for Turbulence Research, Stanford University, Stanford, CA 94305*
[2] *Mechanical Engineering Department, Stanford University, Stanford, CA 94305*
[3] *US Space Force at Rocket Propulsion Division, Air Force Research Laboratory, Edwards AFB, CA 93526*

S1. Reduced chemistry for CH_4/O_2 combustion at near-atmospheric pressures

A 35-step, 12-species reduced mechanism for CH_4/O_2 combustion at near-atmospheric pressures is briefly summarized here. The method for the reduction can be found in Ref. [1], where a similar mechanism was derived for high pressures (10-100 atm) from the Foundational Fuel Chemistry Model (FFCM) [2]. Briefly, a skeletal model was generated first using laminar flame speed, ignition delay, and extinction time as targets. Lumping was carried out to remove quasi-steady state species. The resulting mechanism, FFCMy-12, was tested for laminar flame speed, ignition delay, and extinction time at high pressures, and it was additionally demonstrated in DNS of CH_4/O_2 turbulent premixed flames [1].

During the early stage of the current study, it was recognized that FFCMy-12 could be improved for near-atmospheric pressures, which represents the condition of interest for the present configuration. For this reason, the kinetic parameters were further optimized to improve prediction of ignition time and laminar flame speed at near-atmospheric pressures (0.5-2.0 atm). The optimization procedure employed the method for uncertainty minimization by polynomial chaos expansions (MUM-PCE) described in detail in Refs. [4, 5]. The MUM-PCE minimizes the model prediction uncertainty by optimizing based on an objective function that takes into account a set of targets and prior uncertainties of the rate parameters. The prior uncertainties of the rate parameters were taken from FFCM-1 [3]. The uncertainties for the numerical targets were set to a factor 1.2 for ignition delays and 2.0 cm/s for laminar flame speeds. The model response surfaces were evaluated using a two-layer neural network, as described in detail in Ref. [6]. The training data were obtained by perturbing the input vector using Sobol sampling with a size of 1000 samples per target.

The resulting kinetic parameters of FFCMy-12 for near-atmospheric pressures are provided in Table S1.1. Figure S1.1 shows comparisons between the reduced model and FFCM-1 for predictions of the laminar flame speed and ignition delay of CH_4/O_2 mixtures at atmospheric pressure. The maximum relative errors in the prediction of laminar premixed-flame speed and ignition delay are, respectively, 15% at an equivalence ratio of 0.6 and 60% at an initial temperature of 970 K. Predictions at 0.5 and 2.0 atm lead to similar relative errors (results not shown here for brevity). FFCM-1 is not particularly optimized for CH_4/O_2 combustion because very few data are available for methane oxidation in pure oxygen. For this reason, the agreement shown in Fig. S1.1 is considered to be acceptable for the purposes of this study.

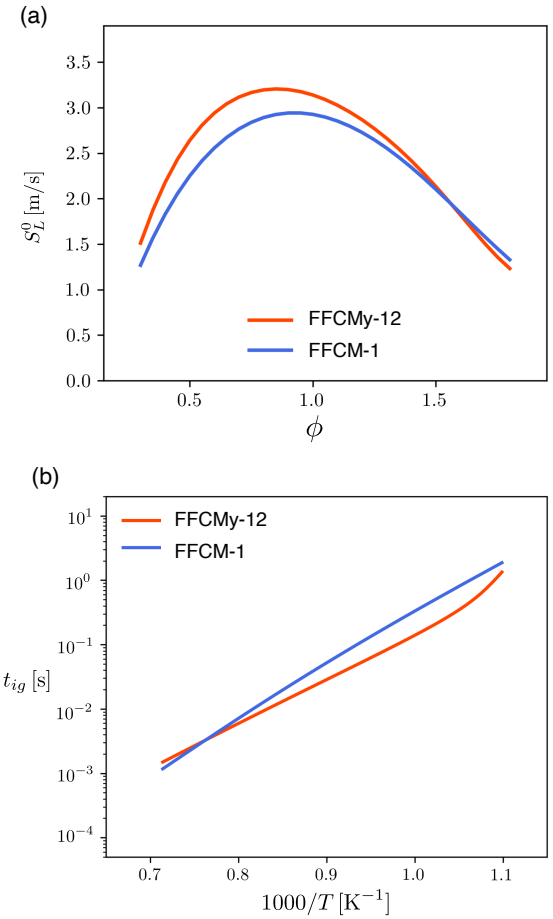

Figure S1.1: Performance of the 12-species reduced mechanism in predicting (a) laminar premixed-flame speed S_L^0 of CH_4/O_2 mixtures as a function of equivalence ratio ϕ at an unburnt gas pressure and temperature of 1 atm and 300 K, respectively, and (b) homogeneous ignition time t_{ig} of an stoichiometric CH_4/O_2 mixture as a function of the inverse of the initial temperature at 1 atm.

Reaction	A	n	E_a
1. $H + O_2 \longleftrightarrow O + OH$	1.002300E+14	0.0	15310.0
2. $H_2 + O \longleftrightarrow H + OH$	3.820000E+12	0.0	7950.0
	5.493800E+14	0.0	19180.0
3. $H_2 + OH \longleftrightarrow H + H_2O$	1.800000E+08	1.51	3437.0
4. $OH + OH \longleftrightarrow H_2O + O$	3.350000E+04	2.42	-1928.0
5. $H_2 + M \longleftrightarrow H + H + M$	4.580000E+19	-1.4	104390.0
Collider effs.: CH_2O: 2.5, CH_4: 2.0, CO: 1.9, CO_2: 3.8, H_2: 2.5, H_2O: 12.0			
6. $O + O + M \longleftrightarrow O_2 + M$	6.160000E+15	-0.5	0.0
Collider effs.: CH_2O: 2.5, CH_4: 2.0, CO: 1.9, CO_2: 3.8, H_2: 2.5, H_2O: 12.0			
7. $H + O + M \longleftrightarrow OH + M$	2.355000E+19	-1.0	0.0
Collider effs.: CH_2O: 2.5, CH_4: 2.0, CO: 1.9, CO_2: 3.8, H_2: 2.5, H_2O: 12.0			
8. $H_2O + M \longleftrightarrow H + OH + M$	6.060000E+27	-3.322	120800.0
Collider effs.: CH_2O: 2.5, CH_4: 7.0, CO: 1.9, CO_2: 3.8, H_2: 3.0, O_2: 1.5			
9. $H_2O + H_2O \longleftrightarrow H + OH + H_2$	3.156300E+25	-2.44	120200.0
10. $H + O_2 + M \longleftrightarrow HO_2 + M$			
High-pressure rate constant:	7.618100E+12	0.44	0.0
Low-pressure rate constant:	3.129100E+21	-1.72	525.0
Troe Fall-off parameters: $\alpha = 0.5$, $T_1 = 90000.0$, $T_2 = 90000.0$, $T_3 = 30.0$			
Collider effs.: CH_2O: 2.5, CH_4: 2.0, CO: 1.9, CO_2: 3.8, H_2: 2.0, H_2O: 14.0, O_2: 0.78			
11. $H + HO_2 \longleftrightarrow H_2 + O_2$	3.680000E+06	2.087	-1455.0
12. $H + HO_2 \longleftrightarrow OH + OH$	7.080000E+13	0.0	300.0
13. $H + HO_2 \longleftrightarrow H_2O + O$	1.450000E+12	0.0	0.0
14. $HO_2 + O \longleftrightarrow O_2 + OH$	1.630000E+13	0.0	-445.0
15. $HO_2 + OH \longleftrightarrow H_2O + O_2$	7.000000E+12	0.0	-1093.0
	2.812500E+14	0.0	10930.0
16. $CO + O + M \longleftrightarrow CO_2 + M$			
High-pressure rate constant:	1.060000E+13	-0.308	6943.0
Low-pressure rate constant:	1.400000E+21	-2.1	5500.0
Collider effs.: CH_2O: 2.5, CH_4: 2.0, CO: 1.9, CO_2: 3.8, H_2: 2.5, H_2O: 12.0			
17. $CO + O_2 \longleftrightarrow CO_2 + O$	2.530000E+12	0.0	47700.0
18. $CO + OH \longleftrightarrow CO_2 + H$	7.050000E+04	2.053	-356.0
	8.640000E+12	-0.664	332.0
19. $CO + HO_2 \longleftrightarrow CO_2 + OH$	1.570000E+05	2.18	17944.0
20. $CH_4 + H \longleftrightarrow CH_3 + H_2$	4.605000E+06	2.5	7588.0
21. $CH_4 + O \longleftrightarrow CH_3 + OH$	2.310000E+08	1.56	8485.0
22. $CH_4 + OH \longleftrightarrow CH_3 + H_2O$	1.000000E+06	2.182	2446.0
23. $CH_3 + H + M \longleftrightarrow CH_4 + M$			
High-pressure rate constant:	9.400000E+13	0.0	0.0
Low-pressure rate constant:	4.233300E+35	-5.57	3818.0
Troe Fall-off parameters: $\alpha = 0.37$, $T_1 = 61.0$, $T_2 = 90000.0$, $T_3 = 3315.0$			
Collider effs.: CH_2O: 2.5, CH_4: 2.0, CO: 1.5, CO_2: 2.0, H_2: 2.0, H_2O: 6.0			
24. $CH_3 + O \longleftrightarrow CH_2O + H$	7.714300E+13	0.0	0.0
25. $CH_3 + O \longrightarrow CO + H + H_2$	2.310000E+13	0.0	0.0
26. $CH_3 + HO_2 \longleftrightarrow CH_4 + O_2$	2.784500E+05	2.35	-1522.0
27. $CH_3 + HO_2 \longrightarrow CH_2O + H + OH$	2.080000E+13,	0.0	-590.0
28. $CH_3 + O_2 \longrightarrow CH_2O + H + O$	2.510000E+12	0.0	28297.0
29. $CH_3 + O_2 \longleftrightarrow CH_2O + OH$	6.840000E+01	2.53	9768.0
30. $CH_2O + CH_3 \longrightarrow CH_4 + CO + H$	1.060000E+01	3.36	4310.0
31. $CH_2O + M \longleftrightarrow CO + H_2 + M$			
High-pressure rate constant:	3.700000E+13	0.0	71980.0
Low-pressure rate constant:	4.400000E+38	-6.1	94000.0
Troe Fall-off parameters: $\alpha = 0.932$, $T_1 = 1540.0$, $T_2 = 10300.0$, $T_3 = 197.0$			
Collider effs.: CH_2O: 2.5, CH_4: 2.0, CO: 1.5, CO_2: 2.0, H_2: 2.0, H_2O: 6.0			
32. $CH_2O + H \longleftrightarrow CO + H_2 + H$	5.670000E+12	0.361	4609.0
	1.140000E+13	0.582	14395.0
33. $CH_2O + O \longrightarrow CO + H + OH$	4.160000E+11	0.57	2762.0
34. $CH_2O + OH \longrightarrow CO + H + H_2O$	7.820000E+07	1.63	-1055.0
35. $CH_2O + O_2 \longrightarrow CO + H + HO_2$	2.440000E+05	2.5	36460.0

Table S1.1: Kinetic parameters for the forward rate constants $k = AT^n \exp[-E_a/(R^0T)]$, with E_a in units of cal/mol and A in units of cm^3/mol·s (for bi-molecular reactions) or cm^6/mol^2·s (for tri-molecular reactions). For reactions with two sets of rate parameters, the rate constant is equal to the sum of the rates computed from the two sets of parameters.

Description	Symbol	Value
x-sponge amplitude	$\mathcal{A}_x$	$4.7U/\delta_{\theta,0} = 25/t_a$
y-sponge amplitude	$\mathcal{A}_y$	$1.2U/\delta_{\theta,0} = 6.3/t_a$
z-sponge amplitude	$\mathcal{A}_z$	$4.7U/\delta_{\theta,0} = 25/t_a$
x-sponge size	w_x	$7.4\delta_{\theta,0} = 0.033L_x = 1.3l_x$
y-sponge size	w_y	$11\delta_{\theta,0} = 0.025L_y$
z-sponge size	w_z	$7.4\delta_{\theta,0} = 0.050L_z = 4.0l_z$
x-sponge duration	$\tau_{s,x}$	$22\delta_{\theta,0}/U = 3.7t_a$
y-sponge duration	$\tau_{s,y}$	$43\delta_{\theta,0}/U = 7.3t_a$
z-sponge duration	$\tau_{s,z}$	$22\delta_{\theta,0}/U = 3.7t_a$

Table S1.2: Sponge boundary-condition parameters applicable to all cases considered in this study.

S2. Method of activation of the sponge boundary condition

The sponge boundary condition described in Sec. 2.6 of the main text is implemented following the method explained in Ref. [7] by including a relaxation term of the form $\sigma(Q_t - Q)$ to the right-hand-side of each of the conservation equations (4)-(6). In this formulation, $Q = \{\rho Y_k, \rho\mathbf{v}, \rho(e + |\mathbf{v}|^2/2)\}$ is the corresponding conserved variable for each equation, and Q_t is the target solution computed from an auxiliary simulation of the turbulent shear layer alone, with neither a kernel nor a sponge. The windowing function $\sigma(x, y, z, t)$ is such that the sponge acts rapidly over short times to absorb the blast wave while the latter crosses a thin region adjacent to the six boundaries of the computational domain.

The specific form of σ is given by $\sigma(x, y, z, t) = \max\{\sigma_x(x, t), \sigma_y(y, t), \sigma_z(z, t)\}$, where

$$\sigma_x(x,t) = \mathcal{A}_x \left[S\left(x; 0, w_x\right) + \mathcal{S}\left(x; L_x, w_z\right) \right] S\left(t; t_{s,x}, \tau_{s,x}\right), \tag{S2.1}$$

$$\sigma_y(y,t) = \mathcal{A}_y \left[\max\left\{ \frac{-3L_y/8 + w_y - y}{w_y}, 0 \right\}^2 + \max\left\{ \frac{y + w_y - 5L_y/8}{w_y}, 0 \right\}^2 \right] \mathcal{S}(t; t_{s,y}, \tau_{s,y}), \tag{S2.2}$$

$$\sigma_z(z,t) = \mathcal{A}_z \left[S\left(z; -\frac{L_z}{2}, w_z\right) + S\left(z; \frac{L_z}{2}, w_z\right) \right] S\left(t; t_{s,z}.\tau_{s,z}\right) \tag{S2.3}$$

are spatiotemporal windowing functions per spatial direction. In this notation, $t_{s,x}$, $t_{s,y}$, and $t_{s,z}$ are the times at sponge activation at the x, y, and z boundaries, respectively. The values of $t_{s,x}$, $t_{s,y}$, and $t_{s,z}$ are chosen such that the sponge along each boundary is activated when the blast wave reaches that bound-

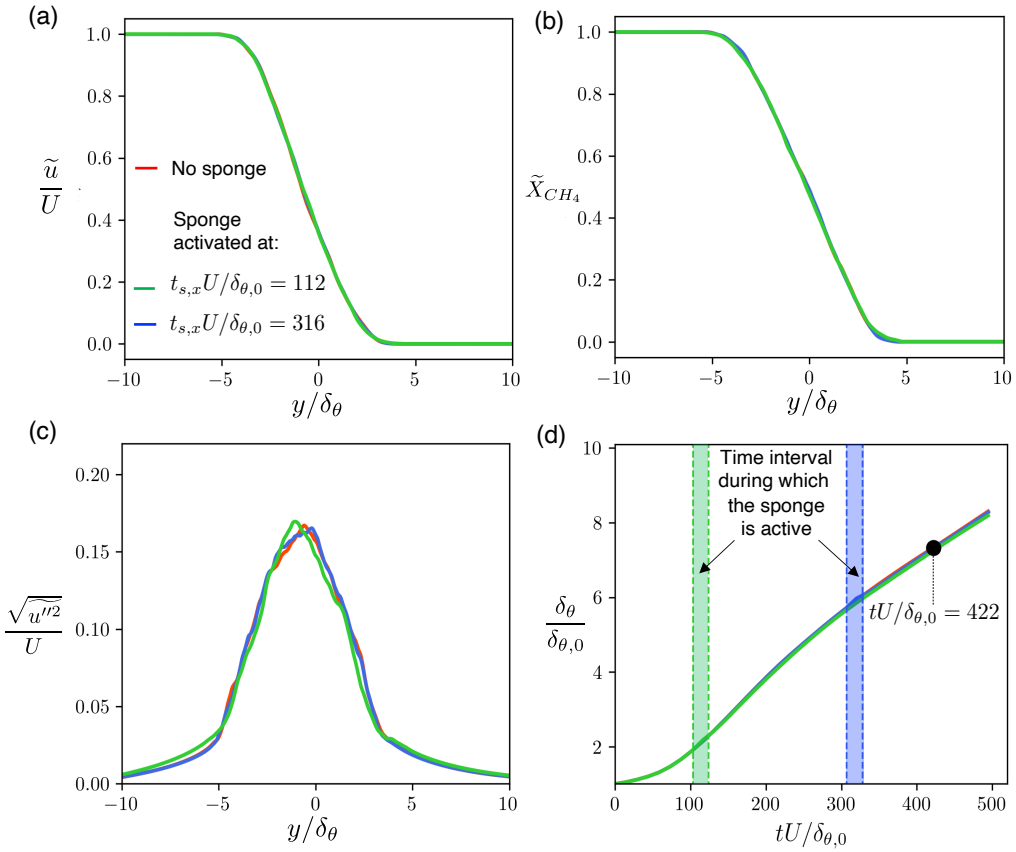

Figure S1.2: Effect of two different sponge activations on (a) mean streamwise velocity, (b) mean molar fraction of fuel, (c) streamwise Reynolds stress, and (d) momentum thickness. Panels (a-c) are evaluated at $tU/\delta_{\theta,0} = 422$ after deactivation of the sponge, as indicated in panel (d). The activation times and durations of the sponges are indicated in panels (a) and (d).

ary. For a given case, these three times differ only slightly in scales of order $\delta_{\theta,0}/U$.

The sponge acts during a relatively short time set by the values of the parameters $\tau_{s,x}$, $\tau_{s,y}$, and $\tau_{s,z}$, which are of the same order as acoustic time based on the length of the computational domain in the corresponding direction. Additionally, $\mathcal{A}_x$, $\mathcal{A}_y$, and $\mathcal{A}_z$ are the amplitudes of the sponge on each boundary. The sponge is active only within a thin region adjacent to the boundaries. The thickness of this region is given by the parameters w_x, w_y, and w_z for each boundary. This thickness is typically less than 5% of the computational domain in the corresponding direction. Values of the sponge amplitudes, activation times, and thicknesses per spatial direction are provided in Table S1.

In Eqs. (S2.1)-(S2.3), the spatio-temporal windowing function $\mathcal{S}$ is given by

$$S(\xi;\xi_0,\Delta) = \frac{1}{2}\tanh\left\{\frac{4m}{\Delta}\left[\xi-\left(\xi_0-\frac{\Delta}{2}\right)\right]\right\} + \frac{1}{2}\tanh\left\{\frac{4m}{\Delta}\left[\xi-\left(\xi_0+\frac{\Delta}{2}\right)\right]\right\}, \tag{S2.4}$$

In particular, $S(\xi;\xi_0,\Delta) = 1$ at $\xi = \xi_0$, whereas $S(\xi;\xi_0,\Delta) \to 0$ smoothly over Δ for both $\xi > \xi_0$ and $\xi < \xi_0$. The constant m is chosen such that $S(\xi_0-p;\xi_0,\Delta) = 0.1$ and $S(\xi_0+p;\xi_0,\Delta) = 0.1$, where p is either the sponge thickness or its duration. The resulting functions $\sigma_x(x,t)$ and $\sigma_z(z,t)$, along with their spatial derivatives, satisfy periodicity across their corresponding boundaries. Similarly, the quadratic increase of σ_y near the outflow boundaries is a standard choice in the literature [7].

Figure S1.2 shows that the time evolution of first- and second-order statistics of the turbulent shear layer are mostly insensitive to the activation and deactivation of the sponge during the time durations employed in this study to dissipate the outgoing blast wave.

S3. Description of supplementary simulation movies

Movies A-F included in this manuscript correspond to meridional ($z = 0$) cross-sections of the DNS results for the six cases described in Table 3 in the main text. Each movie provides the dimensionless density $\rho/\rho_{O_2,\infty}$ (upper left panel), dimensionless temperature T/T_∞ (upper right panel), fuel molar fraction X_{CH_4} (bottom left panel), and dimensionless streamwise velocity $\gamma_{O_2,\infty}^{1/2} u/a_{O_2,\infty}$ (bottom right panel).

References

[1] R. Xu, S.S. Dammati, X. Shi, E.S. Genter, Z. Jozefik, M.E. Harvazinski, T. Lu, A. Poludnenko, V. Sankaran, A.R. Kerstein, and H. Wang. Modeling of high-speed methane-air turbulent combustion - Part II: Reduced methane oxidation chemistry. *Combust. Flame.* (under review), 2023.

[2] Y. Zhang, W. Dong, L. Vandewalle, R. Xu, G. P. Smith, and H. Wang. Foundational Fuel Chemistry Model Version 2.0 (FFCM-2). https://web.stanford.edu/group/haiwanglab/FFCM2", 2023

[3] G. Smith, Y. Tao, and H. Wang. *Foundational Fuel Chemistry Model Version 1.0 (FFCM-1)*, 2016. URL: http://nanoenergy.stanford.edu/ffcm1.

[4] D.A. Sheen and H. Wang. The method of uncertainty quantification and minimization using polynomial chaos expansions. *Combust. Flame.* 158, 2358-2374, 2011.

[5] H. Wang. Uncertainty quantification and minimization. *Comput. Aid. Chem. Eng.* 45, 723- 762, 2019.

[6] Y. Zhang, W. Dong, L.A. Vandewalle, R. Xu, G.P. Smith, and H. Wang. Neural network approach to response surface development for reaction model optimization and uncertainty minimization. *Combust. Flame.* 251, 112679, 2023.

[7] J. B. Freund. Proposed inflow/outflow boundary condition for direct computation of aerodynamic sound, *AIAA J.* 35, 740–742, 1997.